A Micromechanics Based Constitutive Model for Fibre Reinforced Cementitious Composites

Iulia C. Mihai[1*] and Anthony D. Jefferson[1]

[1] Cardiff University, School of Engineering, Queen's Buildings, The Parade CF24 3AA, UK

* Corresponding author. Email: MihaiIC1@cardiff.ac.uk

Abstract

A new constitutive model for fibre reinforced cementitious composites based on micromechanical solutions is proposed. The model employs a two-phase composite based on the Eshelby matrix-inclusion solution and the Mori-Tanaka homogenization scheme and also simulates directional microcracking. An exterior point Eshelby based criterion is employed to model crack-initiation in the matrix-inclusion interface. Microcrack surfaces are assumed to be rough and able to regain contact under both normal and shear displacements. Fibres are included into the formulation in both cracked and uncracked conditions. Once cracks start to develop, the crack-bridging action of fibres is simulated using a local constitutive equation that accounts for the debonding and pull-out of fibre groups with different orientations. It is shown that the combination of the rough microcrack and fibre-bridging sub-models allows microcracking behaviour deriving from both tensile and compressive loads to be modelled in a unified manner. This ability to model tensile and compressive behaviour using the same micromechanical mechanisms is considered to be a particularly attractive feature of the formulation, which removes the need for multi-parameter triaxial yield surfaces and evolution functions that bedevil many competitor models. The model is successfully validated using a series of examples based on experimental test data.

1. Introduction

Over recent decades there has been much research on fibre-reinforced cementitious composites (FRCCs) in order to overcome the main deficiencies of plain concrete, i.e. low tensile strength, low resistance to cracking and relatively brittle behaviour. Today these materials range from conventional fibre-reinforced concrete (FRC), with enhanced toughness and ductility, to high and

ultra high performance fibre-reinforced cementitious composites (HPFRCC and UHFRCC) that exhibit ductile strain-hardening tensile behaviour (Li, 1998; Li, 2003; Naaman, 2011).

In parallel with the development of new FRC materials, and associated experimental investigations, there have also been considerable efforts to develop models to simulate their mechanical behaviour. Early attempts at modelling the constitutive behaviour of FRC focused mainly on specific loading conditions, e.g. uniaxial tension (Lim et al, 1987; Kullaa, 1994; Lange-Kornback and Karihaloo, 1997; Li and Li, 2001) and uniaxial compression (Soroushian and Lee, 1989; Ezeldin and Balaguru, 1992; Barros and Figueiras, 1999; Nataraja et al, 1999). Several macroscopic models have been proposed that consider more general stress states. These often originate from models for plain concrete that have been modified or extended to describe FRC behaviour and tend to make use of continuum damage and/or plasticity theories with an additional component that addresses the crack-bridging effect of fibres (Peng and Meyer, 2000; Luccioni et al, 2012; Hameed et al, 2013). The series of microplane models for plain concrete, developed since the mid 80s by Bažant and co-workers, and others, has been extended for the case of fibre reinforced concrete by Beghini et al. (2007), and Caner et al. (2013). These investigators have included the effect of fibres bridging an open crack by coupling a softening constitutive function for the concrete matrix with a cohesive relationship (Kholmyansky, 2002) that simulates the load resistance of the steel fibres. These models often make use of complex surfaces and evolution functions, usually obtained by fitting experimental data. They also require multiple parameters which can vary significantly when calibrating them using data from different experiments, yet have a strong influence on the predicted behaviour.

Alternatively, models following a mechanics-based approach aim to capture characteristic mechanical behaviour by simulating simple physical mechanisms at the micro or meso-scale. This approach has been applied successfully to modelling the mechanical behaviour of various particulate materials such as metal-matrix composites (Ju and Lee, 2000 and 2001; Ju and Sun, 2001; Sun and Ju, 2001; Chaboche et al, 2001), shape memory alloys (Boyd and Lagoudas, 1996) polymeric and rubber particulate composites (Ravichandran and Liu, 1995) and also geomaterials such as concrete, ceramics and rocks (Ju and Lee, 1991; Lee and Ju, 1991; Gambarotta, 2004; Pensée et al, 2002; Pensée and Kondo, 2003; Abou-Chakra Guéry et al, 2008; Zhu et al., 2008 and 2009; Jefferson and Bennett, 2007 and 2010; Mihai and Jefferson, 2011, Zhu and Shao, 2015; Zhu et al., 2016). Micromechanics based models have also been proposed to simulate time dependent processes in

cement bound materials such as hydration and early age properties (Bernard et al., 2003; Pichler and Hellmich, 2011; Pichler et al., 2013), creep (Pichler and Lackner, 2008) and shrinkage (Pichler et al., 2007; Davies and Jefferson, 2015).

The behaviour of cementitious composites reinforced with randomly distributed and oriented discontinuous fibres is largely governed by fibre pull-out. This may or may not be accompanied by fibre rupture, depending on the fibre geometry and fibre-cement matrix interface properties (Li et al., 1991; Li, 1992). When a crack opens, the fibres crossing it begin to debond and are subsequently pulled out. In this process, they can be considered to apply closure tractions to the crack faces thus stabilising the crack growth. Via these crack-bridging mechanisms, the fibres continue to transfer stresses between the two crack faces until they are completely pulled out. The key factors that influence the crack-bridging effect of fibres and ultimately the overall behaviour of FRC, particularly in the post-cracking stage, are the bond between the fibres and the cementitious matrix and the behaviour of this interface (Wei et al., 1986; Mandel et al., 1987; Naaman et al., 1991b) as well as the dispersion and orientation of fibres (Ferrara et al., 2008; Bolander et al., 2008). For conventional fibre reinforced cementitious composites, that have volume fractions of typically up to 2%, the uniaxial tensile and compressive strengths are only moderately increased; however, the overall toughness and energy absorption capabilities can be increased considerably. High performance and ultra high performance fibre reinforced cementitious composites with increased fibre content (over 2% by volume, typically 6-10%) and carefully engineered cementitious matrices have been developed in more recent years, that have overall superior mechanical properties and dramatically improved behaviour (Habel et al., 2006).

Several models that describe the debonding and pull-out of randomly distributed and oriented short fibres from a cementitious matrix have been proposed (Stang et al., 1990; Li et al., 1991; Li, 1992; Naaman et al., 1991a,b; Lin and Li, 1997). Stang et al. (1990) derived a solution for the problem of an elastic fibre embedded in a rigid matrix assuming that debonding has started and an interfacial crack has developed along part of the fibre-matrix interface. Two criteria for the propagation of debonding were proposed and evaluated; a stress-based and an energy based criterion respectively. Naaman et al. (1991a,b) proposed an analytical model that describes the whole pull-out process of a single fibre aligned with the pull-out force, assuming a linear-elastic – constant frictional bond-slip relationship. Li and co-workers (Li et al., 1991; Li, 1992; Lin and Li, 1997) proposed a series of micromechanics based crack-bridging models that describe the debonding and pull-out of fibres

crossing a crack. The distribution and orientation of fibres relative to the crack-plane was taken into account via probability density functions and closed form solutions were derived for 3-D uniform random distributions and orientation of fibres. In these contributions, a number of assumptions were considered for the fibre-matrix bond model, including constant interface shear stress (Li, 1992), slip-weakening (Li et al., 1991) and slip-hardening behaviour (Li et al., 1991; Lin and Li, 1997). Zhan and Meschke (2014) addressed the pull-out behaviour of steel hooked-end fibres with an analytical model in which the anchorage effects induced by the hooks are evaluated at key pull-out stages that depend on the hook geometry. At each of these key stages the resulting anchorage force was determined from equilibrium of forces and moments, taking into account the damage of concrete and the yielding of steel.

Micromechanics based models describing the crack-bridging action of fibres have also been employed in the material design of fibre reinforced cementitious composites. In the case of ECC, micromechanics principles provided a framework for microstructure tailoring and material optimization in which the material microstructure and associated microparameters that control the behaviour could be identified and subsequently adjusted to obtain desired macroscopic properties and failure behaviour (Li, 1998; Li, 2003). Following this micromechanics based material design theory, Li and co-workers developed a high performance fibre reinforced cementitious composite material which requires only relatively low fibre volume fractions (up to 2%) but which exhibits extensive strain-hardening, has increased strain capacity (up to 6%) and a tensile strength of around 65 MPa (Li, 1998).

Karihaloo and co-workers developed a series of micromechanics based models in which doubly periodic arrays of aligned penny-shaped cracks within an elastic solid are bridged by fibres (Karihaloo et al, 1996; Karihaloo and Wang, 2000). Kabele (2003) proposed a constitutive model to capture the strain-hardening behaviour of ECC in which a relationship between overall stresses and overall strains was derived for a solid Representative Volume Element (RVE) intersected by two mutually perpendicular sets of cracks bridged by fibres. A principal stress criterion governs the initiation of the two sets of cracks that can undergo opening and sliding displacements. The opening and sliding displacements are related to normal and shear tractions through a fibre-bridging crack-plane model that describes the debonding and pull-out of fibres with 3D random distributions and orientations. This model was later applied in a sequential multiscale framework (Kabele, 2007) for modeling the behaviour of ECC in order to describe the overall constitutive relationship of an RVE

containing multiple cracks at a mesoscale level. In the approach proposed by Kabele (2007), four relevant length scales were identified; a macroscale – given by the size of structural elements, mesoscale II – associated with RVEs containing multiple distributed cracks, mesoscale I – associated with the bridging action of fibres across a crack and a microscale – at which the dominant mechanisms are the propagation of cracks from preexisting defects fibre pull-out. Analytical or numerical models were established for each of these length scales and spatial averaging was used to provide the link between consecutive scales. The benefit of such an approach is that the fracture behaviour of the composite can be captured across all these relevant length scales.

Similar benefits are provided by discrete models that simulate explicitly the different phases of the composite (i.e. cementitious matrix, aggregate particles, fibres and their interfaces) and the interaction between them (Bolander and Saito, 1997; Bolander et al., 2008; Radtke et al., 2010; Cunha et al., 2012; Schauffert and Cusatis, 2012; Schauffert et al., 2012; Kang et al., 2014). The key objective of this class of models is the accurate description of the complex micro and meso-structure of fibre reinforced composites and capturing in great detail the dominant physical mechanisms that govern their macroscopic behaviour. While the high computational cost of such models is still a major hindrance to them being extensively applied in the analysis of large scale structural elements, they are very useful for enhancing our understanding of the mechanisms that govern FRC behaviour. Moreover, they can be a valuable tool for the design and development of high performance composites.

A rather different approach was more recently adopted by Oliver et al. (2012) who proposed a micromorphic model that describes the FRC as a combination of three constitutive domains: the concrete matrix, the fibres and the fibre-matrix interface. The model is formulated in the general framework of multifield theory and uses a morphological kinematic descriptor that directly characterizes the fibre-matrix bond slip mechanism. Micromorphic models can be generally classed as macroscopic models but enhanced with information coming from particle interactions occurring at lower scales.

The model proposed in this work builds on a series of micromechanical constitutive models for plain concrete proposed by Jefferson and Bennett (2007, 2010) and Mihai and Jefferson (2011). The present work, aimed at developing a micromechanical model for FRC, represents a major development of these previous models. A particular advantage of the proposed formulation is that microcracking arising from both tensile and compressive loads is treated in a unified fashion. This

means that the model does not need adhoc yield and evolution functions to deal with compressive behaviour, which is in contrast to many other multi-axial models for FRC.

The components of the micromechanical constitutive model which employs Budiansky and O'Connell's (1976) solution for an elastic solid containing penny-shaped microcracks, the Eshelby matrix-inclusion solution (Eshelby, 1957) and which features a microcrack initiation criterion based on the exterior point Eshelby solution as well as a rough crack contact component that accounts for the recovery of stiffness when microcrack surfaces regain contact is summarised in Section 2. The influence of fibres is also addressed in Section 2 in a crack-plane constitutive relationship making use of the crack-bridging stress of Lin and Li (1997). Numerical predictions from single-point simulations of experimental tests in uniaxial tension, uniaxial and compression are presented in Section 3.

2. Constitutive model

2.1. Overall framework

The present formulation builds on a model for plain concrete previously proposed by the authors (Mihai and Jefferson, 2011) which has been extended to address the behaviour of concrete reinforced with randomly distributed short fibres.

The main concepts of the constitutive model are presented in Figure 1. Fibre reinforced concrete is modelled as a two-phase solid material that comprises series of circular cracks which can form in various orientations, defined by ψ and θ (Figure 2). It is assumed that the effect of each series of cracks with the same orientation is equivalent to that of a thin band of material containing these cumulated microcracks (Figure 1b) and, as damage progresses, they can coalesce and form macro-cracks. In this work, the mid-plane of the thin band is referred to as a 'crack-plane'. Furthermore, in each direction, the corresponding crack-plane is crossed by discontinuous fibres, the distribution of which is governed by two probability density functions: the first describing the orientation of the fibres relative to the crack-plane and the other describing the embedment lengths either side of the crack. The model also assumes that cracks have rough surfaces that can regain contact.

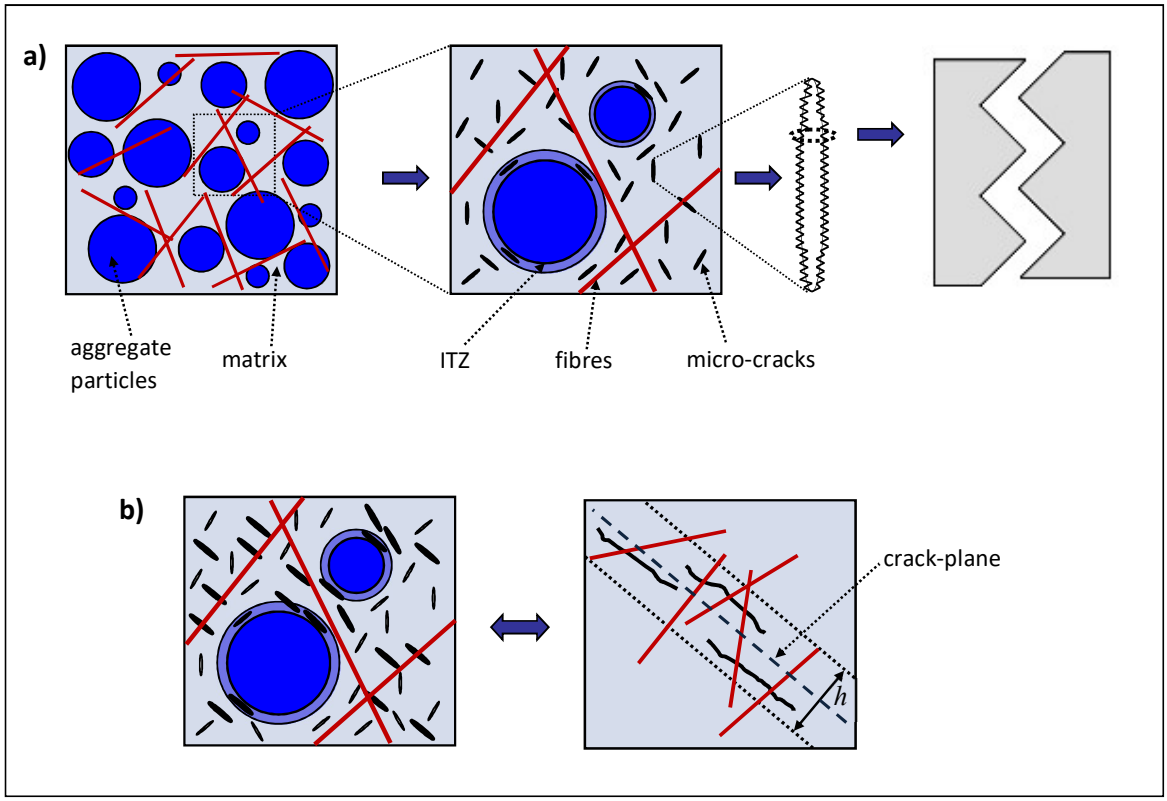

Figure 1. a) Model concepts. b) Schematic representation of the crack-plane

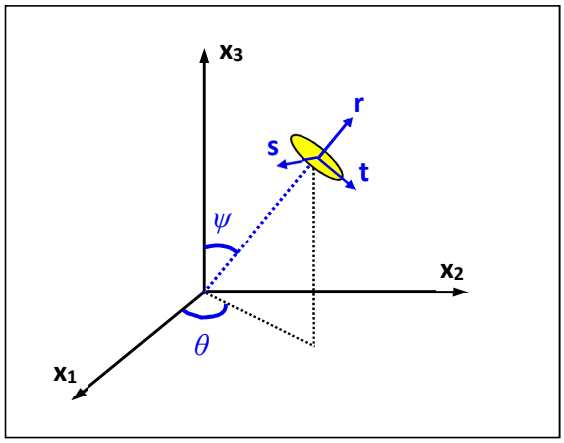

Figure 2. Local coordinate system

The overall constitutive equation takes the following form:

$$\overline{\boldsymbol{\sigma}} = \overline{\mathbf{D}} : \left(\overline{\boldsymbol{\varepsilon}} - \int_{\theta} \int_{\psi} \mathbf{N}_{\varepsilon}(\theta,\psi) : \boldsymbol{\varepsilon}_{\alpha}(\theta,\psi) \mathrm{d}\psi \mathrm{d}\theta \right) \tag{1}$$

in which $\bar{\boldsymbol{\sigma}}$ and $\bar{\boldsymbol{\varepsilon}}$ are the average or far-field stress and stress tensors respectively, $\overline{\mathbf{D}}$ is the homogenized elasticity tensor of the two-phase composite and $\boldsymbol{\varepsilon}_\alpha$ is the added strain tensor from a series of microcracks with the same orientation, written in local coordinates. $\mathbf{N}_\varepsilon$ is a strain transformation tensor such that $\boldsymbol{\varepsilon}_{\mathrm{xyz}} = \mathbf{N}_\varepsilon : \boldsymbol{\varepsilon}_{\mathrm{rst}}$, where $\boldsymbol{\varepsilon}_{\mathrm{xyz}}$ and $\boldsymbol{\varepsilon}_{\mathrm{rst}}$ represent strain tensors in Cartesian and local coordinates respectively.

Once cracks form in a certain direction, stresses are transferred across the corresponding crack-plane via: (i) undamaged material, (ii) rough crack contact or aggregate interlock and (iii) debonding and pull-out of fibres crossing the crack. The model accounts for these load transfer mechanisms through a crack-plane constitutive relation which takes the following generic form:

$$\boldsymbol{\sigma}_{\mathrm{L}} = \boldsymbol{\sigma}_{\mathrm{Lu}} + \boldsymbol{\sigma}_{\mathrm{Lc}} + \boldsymbol{\sigma}_{\mathrm{Lf}} \tag{2}$$

in which:

$\boldsymbol{\sigma}_{\mathrm{Lu}} = h_{\mathrm{u}} \mathbf{D}_{\mathrm{L}} : \boldsymbol{\varepsilon}_{\mathrm{L}}$ *Stress carried by undamaged material*

$\boldsymbol{\sigma}_{\mathrm{Lc}} = h_{\mathrm{d}} \mathbf{D}_{\mathrm{L}} \cdot \mathbf{F}_{\mathrm{c}}(\boldsymbol{\varepsilon}_{\mathrm{L}}) : \boldsymbol{\varepsilon}_{\mathrm{L}}$ *Stress transferred on cracks that regain contact*

$\boldsymbol{\sigma}_{\mathrm{Lf}} = h_{\mathrm{d}} \Psi(V_{\mathrm{f}}) \int_{\varphi}\int_{z} P(\boldsymbol{\varepsilon}_{\mathrm{L}}, \varphi)\mathbf{n}(\varphi)p(\varphi)p(z)\mathrm{d}z\mathrm{d}\varphi$ *Stress transferred by fibres crossing the crack*

and where $\boldsymbol{\sigma}_{\mathrm{L}}$, $\boldsymbol{\varepsilon}_{\mathrm{L}}$ and $\mathbf{D}_{\mathrm{L}}$ are respectively the stress, strain and elasticity tensors on the crack-plane, expressed in the local coordinate system defined by $[\mathbf{r}(\psi,\theta)\ \mathbf{s}(\psi,\theta)\ \mathbf{t}(\psi,\theta)]$; subscript 'L' denotes local or crack-plane quantities and $\mathbf{F}_{\mathrm{c}}$ is a contact tensor. $\Psi(V_f)$ represents the number of fibres crossing a unit crack-plane area, *P* is a fibre pull-out force and $\mathbf{n}$ is a unit vector along the fibre longitudinal axis. $p(\varphi)$ is a probability density function of the fibre orientation angle relative to the crack-plane and $p(z)$ is a probability density function fibre embedment lengths. h_{u} and h_{d} are the proportions of undamaged and cracked material on a particular crack-plane, noting that $h_{\mathrm{u}} + h_{\mathrm{d}} = 1$.

The main components of the model, each of them corresponding to a mechanism, are as follows:

1. ***Two-phase composite***. Concrete is modelled as a two-phase composite that comprises a matrix phase (m) and spherical inclusions (Ω) representing the mortar and the coarse aggregate particles respectively.
2. ***Directional microcracking***. Circular microcracks with various orientations are distributed throughout the composite. For any given orientation, the density of the microcracks is interpreted as a (directional) damage parameter and the initiation of cracking is based on a crack initiation criterion described at point 3.

3. ***Crack initiation***. Damage or cracking in each direction is initiated according to a local principal stress criterion based on an exterior point Eshelby stress distribution. In this work the term 'local' refers to the orientation/direction under consideration.
4. ***Rough crack contact***. The crack faces are assumed to have rough surfaces that can regain contact under normal and shear movement.
5. ***Crack-bridging action of fibres***. As a crack opens, the randomly distributed short fibres that cross the crack-plane undergo debonding and start to pull out from the concrete matrix and during this process they apply closing tractions on the crack faces thus restricting the opening.

2.1. Two-phase composite. Eshelby solution for a spherical inhomogeneity and Mori-Tanaka homogenization.

The homogenised elasticity tensor $\overline{\mathbf{D}}$ (given in Equation 1) is obtained from the elastic properties and the volume fractions of the two phases using the classic Eshelby solution for an ellipsoidal inclusion embedded in an isotropic infinite elastic matrix (Eshelby, 1957) and the Mori-Tanaka averaging method for a non-dilute distribution of inclusions (Mura, 1987):

$$\overline{\mathbf{D}} = \left(f_{\mathrm{m}} \mathbf{D}_{\mathrm{m}} + f_{\Omega} \mathbf{D}_{\Omega} \cdot \mathbf{T}_{\Omega} \right) \cdot \left(f_{\mathrm{m}} \mathbf{I}^{4\mathrm{s}} + f_{\Omega} \mathbf{T}_{\Omega} \right)^{-1} \tag{3}$$

in which $\mathbf{D}_{\mathrm{m}}$ and $\mathbf{D}_{\Omega}$ represent the elasticity tensors of the matrix and the inhomogeneity phase respectively, f_{m} and f_{Ω} are the volume fractions of the two phases with $f_{\mathrm{m}} + f_{\Omega} = 1$, $\mathbf{I}^{4\mathrm{s}}$ is the fourth order identity tensor and $\mathbf{T}_{\Omega}$ is given by:

$$\mathbf{T}_{\Omega} = \mathbf{I}^{4s} + \mathbf{S}_{\Omega} \cdot \left[\left(\mathbf{D}_{\Omega} - \mathbf{D}_{\mathrm{m}} \right) \cdot \mathbf{S}_{\Omega} + \mathbf{D}_{\mathrm{m}} \right]^{-1} \cdot \left(\mathbf{D}_{\mathrm{m}} - \mathbf{D}_{\Omega} \right) \tag{4}$$

where $\mathbf{S}_{\Omega}$ is the Eshelby tensor for spherical inclusions (Nemat-Nasser and Hori, 1993).

2.2. Microcracking. Budiansky and O'Connell solution for circular microcracks.

The added strains resulting from the microcracks are superimposed on the composite such that the constitutive equation becomes:

$$\bar{\boldsymbol{\sigma}} = \bar{\mathbf{D}} : (\bar{\boldsymbol{\varepsilon}} - \boldsymbol{\varepsilon}_a) \tag{5}$$

The overall added strains due to the presence of microcracks is obtained as follows (Nemat-Nasser and Hori, 1993; Budiansky and O'Connell 1976):

$$\boldsymbol{\varepsilon}_a = \frac{1}{2\pi}\int_0^{2\pi}\int_0^{\pi/2} \mathbf{N}_\varepsilon(\psi,\theta) : \boldsymbol{\varepsilon}_\alpha \cdot \sin(\psi)\, \mathrm{d}\psi\, \mathrm{d}\theta \tag{6}$$

where $\boldsymbol{\varepsilon}_\alpha$ is the added strain tensor from a dilute series of microcracks with the same orientation, defined in the local co-ordinates (**r**,**s**,**t**) of the crack (Figure 2). ψ and θ define the orientation of the local coordinates of the microcracks relative to the fixed reference system, with the unit vector normal to the microcrack plane being **r** = ($\sin\psi\cdot\cos\theta$ $\sin\psi\cdot\sin\theta$ $\cos\psi$). The total added strains $\boldsymbol{\varepsilon}_a$ are obtained in the fixed reference configuration by transforming and summing the contributions of microcracks from all orientations. The strain tensor from a dilute series of microcracks with the same orientation is:

$$\boldsymbol{\varepsilon}_\alpha = \mathbf{C}_\alpha(\psi,\theta) : \boldsymbol{\sigma}_L = f(\psi,\theta)\mathbf{C}_{\alpha c} : \boldsymbol{\sigma}_L \tag{7}$$

in which $\boldsymbol{\sigma}_L = (\sigma_{Lrr}\ \sigma_{Lrs}\ \sigma_{Lrt})^T$ is the local stress tensor, $f(\psi,\theta)$ is the crack density parameter introduced by Budiansky and O'Connel (1976) and $\mathbf{C}_{\alpha c}$ is the additional compliance due to the presence of microcracks. In this work, the term 'local' and subscript 'L' refer to quantities in the local co-ordinate system (**r**,**s**,**t**) - shown in Figure 2 - associated with each family of microcracks with the same orientation relative to the Cartesian co-ordinate system ($\mathbf{x}_1$, $\mathbf{x}_2$, $\mathbf{x}_3$).

If $\boldsymbol{\sigma}_L$ and $\boldsymbol{\varepsilon}_\alpha$ are considered in reduced vector forms ($[\sigma_{Lrr}\ \sigma_{Lrs}\ \sigma_{Lrt}]^T$ and = $[\varepsilon_{\alpha rr}\ \gamma_{\alpha rs}\ \gamma_{\alpha rt}]^T$ respectively) containing only the components which can be non-zero, and $\mathbf{C}_{\alpha c}$ is expressed as a matrix relating these local vectors, then, for a dilute series of cracks , $\mathbf{C}_{\alpha c}$ takes the form (Nemat-Naser and Hori, 1993):

$$\mathbf{C}_{\alpha c} = \frac{16(1-\nu_m^{\,2})}{3E_m}\begin{bmatrix} 1 & 0 & 0 \\ 0 & \dfrac{4}{2-\nu_m} & 0 \\ 0 & 0 & \dfrac{4}{2-\nu_m} \end{bmatrix} \tag{8}$$

where E_m and ν_m are the Young's modulus and Poisson's ratio of the matrix phase respectively.

For each orientation the crack density parameter $f(\psi,\theta)$ characterizes the degree of cracking of the crack-plane associated to that direction. In Jefferson and Bennett (2007) the crack density

parameter of Budiansky and O'Connell (1976) – f – was expressed in terms of a directional damage parameter $\omega(\psi,\theta)$, which varies between 0 at no damage and 1 at complete damage, such that:

$$f(\psi,\theta) = \frac{3}{16(1-\nu_m{}^2)} \frac{\omega(\psi,\theta)}{1-\omega(\psi,\theta)} \tag{9a}$$

and

$$\mathbf{C}_\alpha(\psi,\theta) = f(\psi,\theta)\mathbf{C}_{\alpha c} = \frac{\omega(\psi,\theta)}{1-\omega(\psi,\theta)}\mathbf{C}_L \tag{9b}$$

where C_L is the local elastic compliance tensor, the equivalent matrix form of which is

$$\mathbf{C}_L = \frac{1}{E_m}\begin{bmatrix} 1 & 0 & 0 \\ 0 & \dfrac{4}{2-\nu_m} & 0 \\ 0 & 0 & \dfrac{4}{2-\nu_m} \end{bmatrix}.$$

Noting that the local stress ($\boldsymbol{\sigma}_L$) is related to the total stress ($\boldsymbol{\sigma}$) as follows:

$$\boldsymbol{\sigma}_L(\psi,\theta) = \mathbf{N}(\psi,\theta) : \overline{\boldsymbol{\sigma}} \tag{10}$$

where $\mathbf{N}(\psi,\theta)$ is the stress transformation tensor, given in full in Jefferson (2003). Making use of Equations (7) and (9b) and (10), Equation (6) becomes:

$$\boldsymbol{\varepsilon}_a = \frac{1}{2\pi}\left(\int_0^{2\pi}\int_0^{\pi/2} \mathbf{N}_\varepsilon(\psi,\theta) : \frac{\omega(\psi,\theta)}{1-\omega(\psi,\theta)} \cdot \mathbf{C}_L : \mathbf{N}(\psi,\theta) \cdot \sin(\psi) \mathrm{d}\psi \mathrm{d}\theta\right) : \overline{\boldsymbol{\sigma}} \tag{11}$$

Introducing Equation (11) into Equation (3) and rearranging gives:

$$\overline{\boldsymbol{\sigma}} = \left(\mathbf{I}^{4s} + \frac{\overline{\mathbf{D}}}{2\pi}\int_0^{2\pi}\int_0^{\pi/2} \mathbf{N}_\varepsilon(\psi,\theta) : \frac{\omega(\psi,\theta)}{1-\omega(\psi,\theta)} \cdot \mathbf{C}_L : \mathbf{N}(\psi,\theta) \cdot \sin(\psi) \mathrm{d}\psi \mathrm{d}\theta\right)^{-1} \cdot \overline{\mathbf{D}} : \overline{\boldsymbol{\varepsilon}} \tag{12}$$

2.3. Microcrack initiation criterion.

The crack initiation criterion proposed by Mihai and Jefferson (2011) is adopted in the present model; microcracking in each direction is assumed to initiate in a band of matrix material within the interfacial transition zone (ITZ), when the local principal stress in this band reaches the tensile strength of the interface (f_{ti}). It is noted that the band of material is constrained such that the only

non-zero components of the local strain and stress tensors are the *rr*, *rs* and *rt* components. The initial damage surface, F_s is given by:

$$F_s(\boldsymbol{\sigma}_L, f_{ti}) = \sigma_I(\boldsymbol{\sigma}_L) - f_{ti} = 0 \tag{13}$$

The 'exterior point Eshelby' solution (Eshelby, 1959) is employed in evaluating the local stresses in the thin band of matrix material in the ITZ. This solution gives the expression of the total stress field outside an ellipsoidal inclusion embedded in an infinite elastic matrix (Ju and Sun, 1999). The Mori-Tanaka homogenization scheme is applied in order to account for the interaction between inclusions and the total stress field in the matrix outside an inclusion is obtained as:

$$\boldsymbol{\sigma}_{\mathrm{m}\Omega}(\mathbf{x}) = \mathbf{D}_{\mathrm{m}} \cdot \left[\mathbf{I}^{4s} + \mathbf{S}_{\mathrm{E}}(\mathbf{x}) \cdot \mathbf{B}_{\Omega}\right] \cdot \left[f_{\Omega}\mathbf{T}_{\Omega} + f_m\mathbf{I}^{4s}\right]^{-1} : \left(\overline{\boldsymbol{\varepsilon}} - \boldsymbol{\varepsilon}_{\mathrm{a}}\right) \tag{14}$$

in which $\mathbf{B}_{\Omega} = -\left[\mathbf{S}_{\Omega} + \left(\mathbf{D}_{\Omega} - \mathbf{D}_{\mathrm{m}}\right)^{-1} \cdot \mathbf{D}_{\mathrm{m}}\right]^{-1}$.

$\mathbf{S}_{\mathrm{E}}(\mathbf{x})$ is the exterior point Eshelby tensor for spherical inclusions, derived in a dimensionless form in Li et al. (2007) and $\mathbf{x}$ is the position vector relative to the centre of inclusion. In each direction, the local stress in the thin band within the ITZ from Equation (13) is obtained by applying the static constraint from Equation (10) to the expression of the total strain given by Equation (15) for a position **x** located on the matrix-inclusion boundary:

$$\boldsymbol{\sigma}_{\mathrm{Lm}\Omega}(\mathbf{x}, \psi, \theta) = \mathbf{N}(\psi, \theta) : \boldsymbol{\sigma}_{\mathrm{m}\Omega}(\mathbf{x}) \tag{15}$$

and the local strain tensor is:

$$\boldsymbol{\varepsilon}_{\mathrm{Lm}\Omega}(\mathbf{x}, \psi, \theta) = \mathbf{C}_{\mathrm{L}}^{-1} : \boldsymbol{\sigma}_{\mathrm{Lm}\Omega}(\mathbf{x}, \psi, \theta) \tag{16}$$

A local damage function was subsequently derived from the local crack initiation criterion in Equation (13) and is given by:

$$F_{\zeta}(\boldsymbol{\varepsilon}_L, \zeta) = \left(\varepsilon_{Lrr}\frac{1+\alpha_L}{2} + \sqrt{{\varepsilon_{Lrr}}^2\left(\frac{1-\alpha_L}{2}\right)^2 + {r_L}^2\left({\varepsilon_{Lrs}}^2 + {\varepsilon_{Lrt}}^2\right)}\right) - \zeta \tag{17}$$

in which $\alpha_{\mathrm{L}} = \frac{\nu_{\mathrm{m}}}{1-\nu_{\mathrm{m}}}$, $r_{\mathrm{L}} = \frac{\nu_{\mathrm{m}} - 1/2}{\nu_{\mathrm{m}} - 1}$ and noting that the following loading/unloading conditions apply:

$$F_{\zeta} \le 0; \quad \dot{\zeta} \ge 0; \quad F_{\zeta}\dot{\zeta} = 0 \tag{18a,b,c}$$

It was shown in Mihai and Jefferson (2011) that when the composite is subjected to uniaxial compressive stresses, the expression of the stress field in the matrix phase outside the inclusion in Equation (14) captures sharp gradients and tensile stress concentrations in a lateral direction and in a region adjacent to a matrix-inclusion interface. In a comparative study, Davies and Jefferson (2015) showed a very good agreement between the exterior point Eshelby solution and a finite element solution of a matrix domain with a finite set of inclusions. The two-phase composite description of the material combined with the exterior point Eshebly crack initiation criterion allows the model to simulate compressive splitting cracks naturally.

Once damage is initiated in a certain direction, the evolution of the damage parameter is based on a standard exponential tensile softening function given by:

$$\omega = 1 - \frac{\varepsilon_{\mathrm{tm}}}{\zeta} \cdot e^{-c_1 \frac{\zeta - \varepsilon_{\mathrm{tm}}}{\varepsilon_0 - \varepsilon_{\mathrm{tm}}}} \tag{19}$$

where $\varepsilon_{\mathrm{tm}}$ is the matrix strain at first damage, given by $\varepsilon_{\mathrm{tm}} = f_{\mathrm{ti}}/E_{\mathrm{m}}$ and $\varepsilon_0 = u_0/h$, where u_0 is the relative displacement at the effective end of the uniaxial tensile softening curve; c_1 (=5) controls the shape of the uniaxial tensile softening branch and *h* is a length parameter assumed equal to the width of the fracture process zone (Bažant and Oh, 1983).

2.4. Rough crack contact

Various studies of micrographs of fractured concrete specimens at micro and meso levels show that cracks in cementitious materials have rough opposing surfaces (Zampini et al., 1995; Issa et al, 2003; Nichols and Lange, 2006) and these can come into contact not only when the crack closes but also under combinations of shear and opening displacements. Therefore a model that takes into account the tortuous nature of crack surfaces is likely to give more realistic predictions. The rough contact crack-plane model (Jefferson 2002, Mihai and Jefferson, 2013), written in stress – relative displacement terms, considers crack-plane strains as follows:

$$\begin{bmatrix} \varepsilon_{\mathrm{rr}} & \varepsilon_{\mathrm{rs}} & \varepsilon_{\mathrm{rt}} \end{bmatrix}^{\mathrm{T}} = \frac{1}{h} \begin{bmatrix} u_{\mathrm{r}} & u_{\mathrm{s}} & u_{\mathrm{t}} \end{bmatrix}^{\mathrm{T}} \tag{20}$$

It is assumed that in each direction the local stress that is transferred across a crack-plane has an undamaged and a damaged component respectively, as illustrated in Figure 3**.** The undamaged

component represents the average stresses on intact material whereas the damaged component describes the recovered stress on damaged material that regains contact.

$$\boldsymbol{\sigma}_{\mathrm{L}} = (1-\omega(\psi,\theta))\boldsymbol{\sigma}_{\mathrm{Lu}} + \omega(\psi,\theta)\boldsymbol{\sigma}_{\mathrm{Lc}} \tag{21}$$

in which:

$$\boldsymbol{\sigma}_{\mathrm{Lu}} = \mathbf{C}_{\mathrm{L}}^{-1} : \boldsymbol{\varepsilon}_{\mathrm{L}} \tag{22}$$

and the stress recovered when the cracks regain contact, $\boldsymbol{\sigma}_{\mathrm{Lc}}$ is proportional to a so called embedment strain $\mathbf{g}$ (Figure 4) – which in turn depends on the state of contact – as follows:

$$\boldsymbol{\sigma}_{\mathrm{Lc}} = H(\boldsymbol{\varepsilon}_L)\mathbf{C}_{\mathrm{L}}^{-1} : \mathbf{g} \tag{23}$$

Equation (21) is equivalent to the first two terms in Equation (2) for which $h_u = 1 - \omega$ and $h_d = \omega$.

The embedment strain $\mathbf{g}$ is obtained by the following transformation of the local strain:

$$\mathbf{g} = \boldsymbol{\Phi}(m_g, \boldsymbol{\varepsilon}_L) : \boldsymbol{\varepsilon}_L \tag{24}$$

where $\boldsymbol{\Phi}(m_g, \boldsymbol{\varepsilon}_{\mathrm{L}})$ is a contact matrix that depends upon the contact state. Three contact states are considered in the model; open, interlock or closed (Figure 4). The contact regions are delimited by two contact surfaces – the interlock surface ($\phi_{\mathrm{int}} = 0$) and the closed surface ($\phi_{cl} = 0$) given below:

$$\begin{aligned} \phi_{\mathrm{int}}(\boldsymbol{\varepsilon}_{\mathrm{L}}, m_g) &= m_g \varepsilon_{Lrr} - \sqrt{\varepsilon_{Lrs}{}^2 + \varepsilon_{Lrt}{}^2} = 0 \\ \phi_{\mathrm{cl}}(\boldsymbol{\varepsilon}_{\mathrm{L}}, m_g) &= \varepsilon_{Lrr} + m_g \sqrt{\varepsilon_{Lrs}{}^2 + \varepsilon_{Lrt}{}^2} = 0 \end{aligned} \tag{25}$$

in which m_g is the slope of the interlock surface and represents, in a physical sense, the slope of the asperity, thus being a measure of the crack surface roughness. The mathematical description of the contact model is given in Table 1.

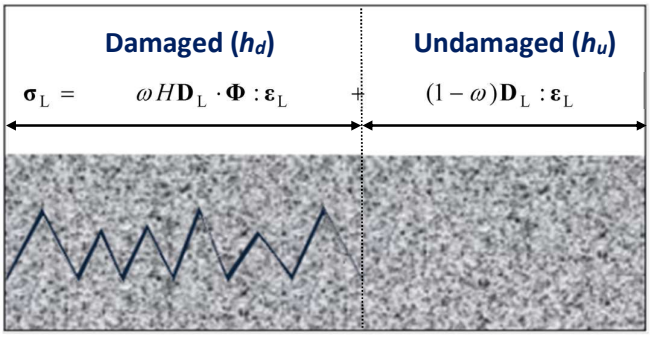

Figure 3. Rough crack contact illustration

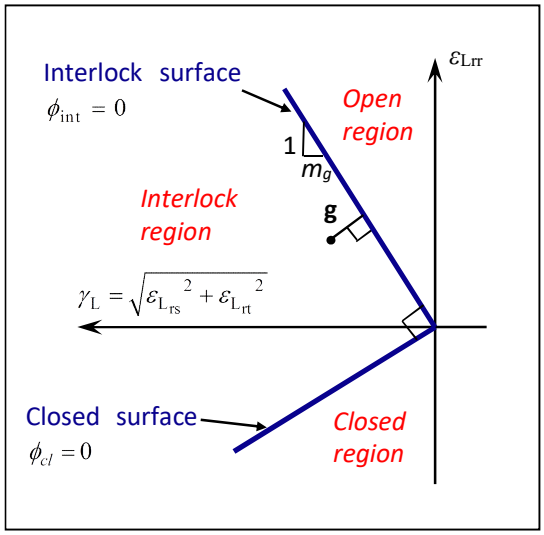

Figure 4. Contact surfaces and contact states

Table 1. Contact formulation

Region	Contact state	Contact matrix ($\boldsymbol{\Phi}=$)
$\phi_{int}(\boldsymbol{\varepsilon}_L, m_g) \geq 0$	Open	$\mathbf{0}^{2s}$
$\phi_{int}(\boldsymbol{\varepsilon}_L, m_g) < 0$ & $\phi_{cl}(\boldsymbol{\varepsilon}_L, m_g) > 0$	Interlock	$\frac{1}{1+m_g^2}\left(\left(\frac{\partial \phi_{int}}{\partial \boldsymbol{\varepsilon}_L}\right)\left(\frac{\partial \phi_{int}}{\partial \boldsymbol{\varepsilon}_L}\right)^T + \frac{\partial^2 \phi_{int}}{\partial \boldsymbol{\varepsilon}_L^2}\right)$
$\phi_{cl}(\boldsymbol{\varepsilon}_L, m_g) \leq 0$	Closed	$\mathbf{I}^{2s}$

$H(\boldsymbol{\varepsilon}_L)$ in Equation (23) is a contact reduction function that accounts for the reducing potential for shear contact between opposing rough crack surfaces as the crack opening increases. The contact reduction function, derived from geometrical considerations in Mihai and Jefferson (2011, 2013), decreases from 1 to 0 and is given by:

$$H(\boldsymbol{\varepsilon}_L) = e^{-3\frac{\varepsilon_{L11} - \varepsilon_{ti}}{\varepsilon_g}} \tag{26}$$

where $\varepsilon_g = h_t / h$ is the relative asperity height, in which h_t is the height of the asperities

As in previous work, the roughness of the crack surface is assumed to be variable, i.e. the asperities on the crack surfaces have various relative heights (ε_g) and slopes (m_g) (Mihai and Jefferson, 2011; Mihai and Jefferson, 2013). The roughness variation can be introduced through a probability density function $p_c\ (\varepsilon_g, m_g)$ and the stress recovered through contact has the following expression:

$$\boldsymbol{\sigma}_{\mathrm{Lc}} = \mathbf{C}_{\mathrm{L}}{}^{-1} \cdot \left(\int_{\varepsilon_g} \int_{m_g} p_c(\varepsilon_g, m_g) H(\boldsymbol{\varepsilon}_{\mathrm{L}}, \varepsilon_g) \boldsymbol{\Phi}(\boldsymbol{\varepsilon}_{\mathrm{L}}, m_g) \mathrm{d}m_g \mathrm{d}\varepsilon_g \right) : \boldsymbol{\varepsilon}_{\mathrm{L}} \tag{27}$$

A discrete probability distribution was employed in the current work, full details of which are provided in Section 3.1.

Taking into account Equations (22-24) and Equation (27), Equation (21) becomes:

$$\boldsymbol{\sigma}_{\mathrm{L}}(\psi, \theta) = \mathbf{C}_{\mathrm{L}}{}^{-1} \cdot \left[\left(1 - \omega(\psi, \theta)\right) \mathbf{I}^{2s} + \omega(\psi, \theta) \cdot \int_{\varepsilon_g} \int_{m_g} p_c(\varepsilon_g, m_g) H(\boldsymbol{\varepsilon}_{\mathrm{L}}, \varepsilon_g) \boldsymbol{\Phi}(\boldsymbol{\varepsilon}_{\mathrm{L}}, m_g) \mathrm{d}m_g \mathrm{d}\varepsilon_g \right] : \boldsymbol{\varepsilon}_{\mathrm{L}} \tag{28}$$

To include the rough contact into the model $\mathbf{C}_{\alpha}(\psi, \theta) = \dfrac{\omega(\psi, \theta)}{1 - \omega(\psi, \theta)} \mathbf{C}_{\mathrm{L}}$ in Equation (12) is replaced with the added compliance $\mathbf{C}_{\mathrm{c}\alpha}$, obtained by inverting Equation (28) and removing the elastic compliance, which gives:

$$\mathbf{C}_{c\alpha}(\psi, \theta) = \left[\left(\left(1 - \omega(\psi, \theta)\right) \mathbf{I}^{2s} + \omega(\psi, \theta) \cdot \int_{\varepsilon_g} \int_{m_g} p_c(\varepsilon_g, m_g) H(\boldsymbol{\varepsilon}_{\mathrm{L}}, \varepsilon_g) \boldsymbol{\Phi}(\boldsymbol{\varepsilon}_{\mathrm{L}}, m_g) \mathrm{d}m_g \mathrm{d}\varepsilon_g \right)^{-1} - \mathbf{I}^{2s} \right] : \mathbf{C}_{\mathrm{L}} \tag{29}$$

2.5. Local constitutive relationship. Influence of fibres

The influence of randomly distributed short fibres on the mechanical behaviour of FRC is now addressed. The incorporation of short fibres into cement-based composites leads to an improvement of their mechanical properties.

The underlying mechanism that causes this improved behaviour is fibre debonding and pull-out. When a crack opens the fibres crossing the crack-plane begin to debond from the concrete matrix and are subsequently pulled out (i.e. the fibres slide relative to the concrete matrix). Throughout

this process, the fibres apply closure tractions on the crack faces. Via these crack-bridging mechanisms, the fibres continue to transfer stresses between the two crack faces until they are completely pulled out.

The effect of fibres under uncracked conditions is taken into account on the elastic modulus according to the law of mixtures, with the fibre component being derived from a three-dimensional random fibre network as presented in Garg et al. (1973):

$$E_{FRC} = \frac{E_f V_f}{6} + \bar{E}(1 - \frac{V_f}{6}) \tag{30}$$

in which E_{FRC} is the Young's moduli of the undamaged FRC, E_f is the Young's moduli of fibres, a, $\bar{E}$ is the elastic modulus consistent with the homogenised elasticity tensor $\bar{\mathbf{D}}$ in Equation (3) and V_f is the volume fraction of the fibres. It is noted that the addition of fibres in relatively limited amounts, as is the case for conventional FRC, has a second order effect on the effective elastic properties.

The bridging influence of fibres is taken into account through the third term in the local or crack-plane constitutive relation, $\boldsymbol{\sigma}_{Lf}$, given in a general form in Equation (2). Since the bridging effect of fibres becomes significant only after crack formation, the stress transferred across the crack through the debonding and pull-out of fibres is multiplied by the proportion of damaged material on the crack-plane under consideration, h_d. This concept is illustrated in Figure 5.

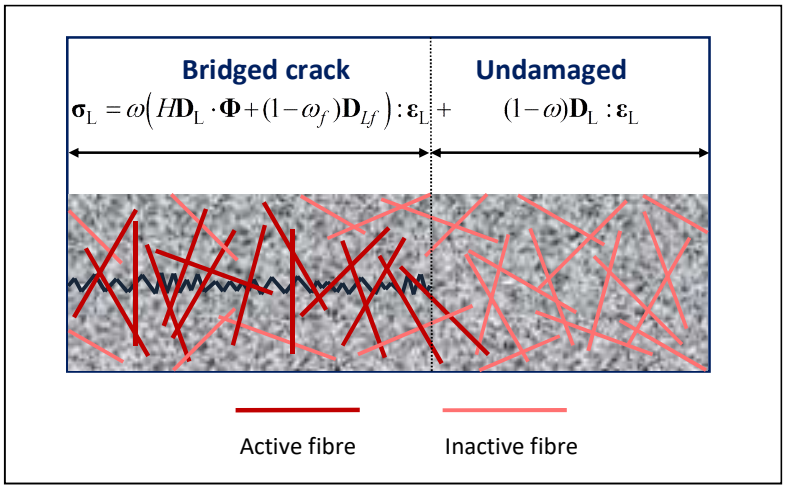

Figure 5. Crack-plane model with rough contact and fibre-bridging

It was found convenient to write the stress transferred via the fibres in the following form:

$$\boldsymbol{\sigma}_{\mathrm{Lf}} = \left(1-\omega_f(\psi,\theta)\right)\mathbf{D}_{\mathrm{Lf}} : \boldsymbol{\varepsilon}_{\mathrm{L}} \tag{31}$$

where ω_f is a fibre effective damage parameter that characterises the crack-bridging state of fibres and varies from 0, for a state before any fibre pull-out occurs, to 1, for a case in which all fibres are completely pulled out from the matrix.

$\mathbf{D}_{\mathrm{Lf}}$ is a local elastic stiffness given by the interface bond of the fibres crossing the crack-plane, before the start of pull-out, assuming a linear debonding behaviour. It is also assumed that the bending stiffness or the dowel action of the fibres is negligible and that the fibres deform in accordance with the resultant crack opening (Figure 6). This is true particularly for fibres with a small diameter, high aspect ratio and a relatively reduced elastic modulus such as some polyethylene and polypropylene fibres. However, for the case of steel fibres the model will slightly undersestimate the shear force transferred across a micro crack and therefore, in this sense, the assumption is considered mildly conservative.

Taking this into account, $\mathbf{D}_{\mathrm{Lf}}$ is isotropic and takes the following form:

$$\mathbf{D}_{\mathrm{Lf}} = E_{df} \cdot \mathbf{I}^{2\mathrm{s}} \tag{32}$$

where E_{df} is an effective elastic modulus that will be determined in due course.

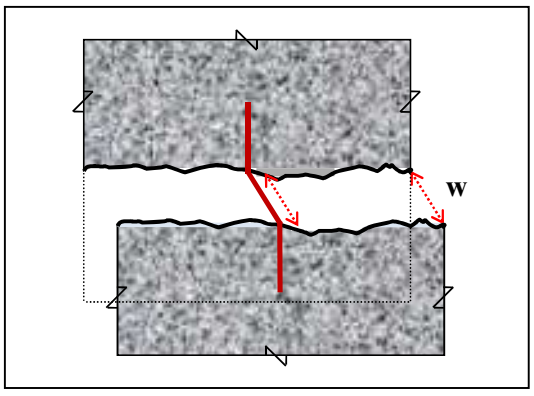

Figure 6. Negligible dowel action of fibres

The evolution of the fibre effective damage parameter ω_f is obtained from the following 1-D relation:

$$(1-\omega_f)E_{df}\zeta_f = \sigma_{cb} \tag{33}$$

in which ζ_f is a resultant crack opening parameter that takes into account the normal and shear components of the crack-plane strain tensor and is governed by the effective fibre damage function given in Equation (34) and the loading/unloading conditions given in Equations (35 a,b,c):

$$F_{\zeta f}(\boldsymbol{\varepsilon}_L, \zeta_f) = \frac{1}{2}\left(\varepsilon_{Lrr} + \sqrt{{\varepsilon_{Lrr}}^2 + 4\left({\varepsilon_{Lrs}}^2 + {\varepsilon_{Lrt}}^2\right)}\right) - \zeta_f \tag{34}$$

$$F_{\zeta f} \le 0; \quad \dot{\zeta}_f \ge 0; \quad F_{\zeta f}\dot{\zeta}_f = 0 \tag{35 a,b,c}$$

σ_{cb} in Equation (33) is the stress that is transferred between two opposing faces of a fully formed crack subjected to normal opening displacements, through the pull-out action of the fibres that cross the crack. In general, the crack-bridging stress depends upon the density of fibres crossing the crack, the geometry of fibres (i.e. length L_f, diameter d_f and shape), the fibre material properties (in particular tensile strength, f_{tf} and Young's modulus, E_f), the orientation of the fibres relative to the crack-plane, the embedment lengths either side of the crack-plane and the nature of the bond between the fibres and the cementitious matrix. The crack-bridging stress can be determined by integrating the individual contributions from those fibres that cross the crack-plane (Li et al., 1991). For fibre reinforced concrete, in which the fibres are randomly distributed and oriented, a general expression for the crack-bridging stress in relative displacements terms can be written as:

$$\sigma_{\mathrm{cb}}(w) = \frac{N_f}{A_{cp}} \int_{\varphi}\int_{z} P_f(\varphi, z, \boldsymbol{\Theta}, \mathbf{b}, w) \cdot p(\varphi) \cdot p(z) \mathrm{d}\varphi \mathrm{d}z \tag{36}$$

where N_f is the number of fibres crossing the crack-plane of area A_{cp}, and depends upon the volume fraction of fibres in the composite (V_f) and their cross-sectional area. w is the normal opening displacement, P_f is the pull-out force carried by a single fibre, φ is the orientation angle of the fibre relative to the crack-plane, z is the distance between the centroid of the fibre and the crack-plane. $\boldsymbol{\Theta}$ represents the set of properties related to the material and geometry of fibres, including the shape of fibres - e.g. straight, crimped, with hooked ends etc - and $\mathbf{b}$ represents the set of fibre-matrix bond properties. $p(\varphi)$ and $p(z)$ denote probability density functions of the fibre orientation angle and centroidal distance to the crack-plane respectively. Noting that the volume fraction of fibres is $N_f = \frac{V_f A_{cp}}{A_f}$, Equation (36) becomes:

$$\sigma_{\mathrm{cb}}(w) = \frac{4V_f}{\pi {d_f}^2} \int_{\varphi}\int_{z} P_f(\varphi, z, \boldsymbol{\Theta}, \mathbf{b}, w) \cdot p(\varphi) \cdot p(z) \mathrm{d}\varphi \mathrm{d}z \tag{37}$$

Experiments show that the single fibre pull-out force increases for increasing fibre inclination angle φ, a phenomenon called 'snubbing effect'. According to Li et al. (1990), the force required to pull out a fibre with an inclination angle φ is:

$$P_f(\varphi) = e^{f_s \varphi} P_{f0} \tag{38}$$

where $P_{f0} = P_f(\varphi{=}0)$, φ is expressed in radians and f_s is a snubbing coefficient that depends upon the type of fibres and the strength of matrix.

The pull-out behaviour of a single fibre can be measured experimentally and the pull-out force – displacement curve used directly in Equation (37). Several fibre pull-out models have been proposed, that employ mechanics (e.g. Li et al., 1991; Li, 1992; Naaman et al., 1991a,b; Lin and Li, 1997) or fracture mechanics theories (e.g. Stang et al., 1990). The mechanics-based model proposed by Lin and Li (1997) was adopted here. The pull-out model uses a linear slip-hardening constitutive relation (Equation 39) between the fibre-matrix interface shear stress (τ) and the interface slip (S) in deriving the pull-out force of a single, straight fibre aligned with the force.

$$\tau = \tau_0 (1 + \beta S / d_f) \tag{39}$$

in which τ_0 is the frictional sliding shear stress at the tip of the debonding zone before any slip takes place and β is a nondimensional hardening parameter. The two fibre-matrix interface parameters, τ_0 and β can be obtained from an experimental single fibre pull-out P-δ curve, as detailed in Lin and Li (1997).

Assuming that the disposition of fibres is completely random within the matrix (i.e. $p(\varphi) = \sin(\varphi)$ and $p(z) = 2/L_f$) and that only the shorter of the two fibre ends either side of the crack-plane debonds and pulls out without breaking, Lin and Li (1997) obtained the following analytical solution for the crack-bridging stress in terms of a normalized crack opening parameter ($\tilde{w}$):

$$\sigma_B(\tilde{w}) = \sigma_0 \cdot \begin{cases} \dfrac{2}{k}\left\{\left[1 - \dfrac{1}{k}\cosh^{-1}\left(1 + \lambda\dfrac{\tilde{w}}{\tilde{w}_{df}}\right)\right]\sqrt{\left(1 + \lambda\dfrac{\tilde{w}}{\tilde{w}_{df}}\right)^2 - 1} + \dfrac{\lambda}{k}\dfrac{\tilde{w}}{\tilde{w}_{df}}\right\} & , \quad 0 \le \tilde{w} \le \tilde{w}_{df} \\ \left(1 + \dfrac{\beta L_f}{2d_f}\tilde{w}\right)\cdot(1-\tilde{w})^2 & , \quad \tilde{w}_{df} < \tilde{w} \le 1 \\ 0 & , \quad \tilde{w} > 1 \end{cases} \tag{40}$$

in which:

$$\tilde{w}=\frac{w}{L_f/2},\qquad \sigma_0=0.5g_s\tau_0V_f(1+\eta_f)\frac{L_f}{d_f},\qquad k=\varpi\frac{L_f}{2d_f},\qquad \lambda=\cosh(k)-1,\qquad \eta_f=\frac{V_fE_f}{(1-V_f)\overline{E}},$$

$\varpi=\sqrt{4(1+\eta_f)\beta\tau_0/E_f}$, $\tilde{w}_{df}=\frac{w_{df}}{L_f/2}$, $w_{df}=\frac{2d_f}{\beta}\cdot\left(\cosh(k)-1\right)$ and g_s is a snubbing factor, given by Equation (41), which in turn depends upon a snubbing coefficient f_s:

$$g_s=\frac{2}{4+f_s^2}\left(1+e^{\pi f_s/2}\right) \tag{41}$$

Equation describes the crack-bridging behaviour of fibres crossing a crack-plane as they debond ($0\le\tilde{w}\le\tilde{w}_{df}$) and are subsequently pulled out ($\tilde{w}_{df}<\tilde{w}\le1$) from the cementitious matrix. In this work it is assumed that the debonding phase is linear elastic and the pull-out phase is governed by the solution obtained by Lin and Li (1997). Therefore, the following apply to Equation (32):

$$E_{df}=\frac{\sigma_0}{\varepsilon_{df}}\left(1+\frac{\beta L_f}{2d_f}\varepsilon_{df}\right)\cdot(1-\varepsilon_{df})^2 \tag{42}$$

and

$$\sigma_{\mathrm{cb}}(\zeta_f)=\begin{cases}E_{df}\zeta_f & ,\quad 0\le\zeta_f\le\varepsilon_{df}\\ \sigma_0\left(1+\dfrac{\beta L_f}{2d_f}\zeta_f\right)\cdot(1-\zeta_f)^2 & ,\quad \varepsilon_{df}<\zeta_f\le\varepsilon_{pf}\\ 0 & ,\quad \varepsilon_{pf}<\zeta_f\end{cases} \tag{43}$$

where $\varepsilon_{df}=\frac{w_{df}}{h}$ and $\varepsilon_{pf}=\frac{L_{\mathrm{f}}/2}{h}$

For the modest fibre volume considered here (V_f ≤ 2%), uniaxial tensile experiments on FRC specimens suggest that strains localise soon after the peak stress is reached (Gopalaratnam and Shah, 1987; Li et al., 1998). The strains localise into a region with a size similar to that of the maximum size of coarse aggregate particles (d_{agg}). Therefore for the present purposes it is assumed that the width of the fracture process zone is $h = 2\cdot d_{agg}$. It is acknowledged that FRC with higher volume fractions exhibit strain hardening, rather than softening behaviour, for which microcracks are distributed and strain localisation is delayed (Naaman, 2011).

It is noted that other pull-out models can be employed in Equation (37) as well as different probability density functions. Indeed, if information on the distribution and orientation of fibres

exists, it can be readily taken into account in the general expression of the crack-bridging stress and if an analytical solution cannot be obtained, the double integral can be determined numerically.

The influence of fibres is taken into account in the local or crack-plane stress – strain expression assuming that the fibre contribution develops after crack initiation. In the case of fibre reinforced concrete Equation (28) becomes:

$$\boldsymbol{\sigma}_{\mathrm{L}} = \left[\left(1-\omega\right)\mathbf{C}_{\mathrm{L}}{}^{-1} + \omega\mathbf{C}_{\mathrm{L}}{}^{-1} \cdot \int_{\varepsilon_g} \int_{m_g} p_c(\varepsilon_g, m_g) H(\boldsymbol{\varepsilon}_{\mathrm{L}}, \varepsilon_g) \boldsymbol{\Phi}(\boldsymbol{\varepsilon}_{\mathrm{L}}, m_g) \mathrm{d}m_g \mathrm{d}\varepsilon_g + \omega(1-\omega_f)\mathbf{D}_{\mathrm{fl}} \right] : \boldsymbol{\varepsilon}_{\mathrm{L}} \quad (44)$$

in which the dependencies of ω and ω_f are dropped for clarity. The final stress-strain model can therefore be written as follows:

$$\overline{\boldsymbol{\sigma}} = \left(\mathbf{I}^{4\mathrm{s}} + \frac{\overline{\mathbf{D}}}{2\pi} \int_0^{2\pi} \int_0^{\pi/2} \mathbf{N}_{\varepsilon}(\psi, \theta) : \mathbf{C}_{add}(\psi, \theta) : \mathbf{N}(\psi, \theta) \cdot \sin(\psi) \mathrm{d}\psi \mathrm{d}\theta \right)^{-1} \cdot \overline{\mathbf{D}} : \overline{\boldsymbol{\varepsilon}} \quad (45)$$

where

$$\mathbf{C}_{\mathrm{add}} = \left[\mathbf{C}_{\mathrm{L}}{}^{-1} \cdot \left[\left(1-\omega\right)\mathbf{I}^{2\mathrm{s}} + \omega \cdot \int_{\varepsilon_g} \int_{m_g} p_c(\varepsilon_g, m_g) H(\boldsymbol{\varepsilon}_{\mathrm{L}}, \varepsilon_g) \boldsymbol{\Phi}(\boldsymbol{\varepsilon}_{\mathrm{L}}, m_g) \mathrm{d}m_g \mathrm{d}\varepsilon_g \right] + \omega(1-\omega_f)\mathbf{D}_{\mathrm{fl}} \right]^{-1} - \mathbf{C}_{\mathrm{L}} \quad (46)$$

The spherical integration in Equation (45) is evaluated numerically by employing McLaren's integration rule with 50 sample directions (Stroud, 1971). The sensitivity of the model with respect to the integration rule is shown in Section 3.6

3. Numerical simulations

The capability of the proposed model to capture the characteristic response in tension and compression of fibre reinforced composites is evaluated in a series of numerical simulations.

Example 1 presents simulations of the uniaxial tension tests of Li et al. (1998) of plain and fibre reinforced concrete specimens with different types of fibres and various fibre contents.

In Example 2 numerical predictions of the uniaxial compression experimental results of Cachim et al. (2002) are presented.

Example 3 presents a comparison of experimental and numerical biaxial compression strength envelopes.

3.1. Model parameters

A summary of the model parameters and how they relate to the mechanistic components of the model presented in Sections 2.2-2.6 is provided here along with some recommended values. Four categories can be distinguished as follows:

a) Elastic material properties related to the two-phase composite solution (Section 2.2); the Young's modulus and Poisson's ratio of the mortar matrix (E_m, ν_m), the Young's modulus and Poisson's ratio of the coarse aggregate particles (E_Ω, ν_Ω) and the volume fractions of the mortar and inclusion phase respectively (f_m and f_Ω). Values for the moduli of elasticity can vary considerably and typical ranges for mortar are 20-32GPa (Yang, 1998). If not reported in the experimental data, they can be chosen such that the elastic modulus of two-phase composite matches the initial slope of the stress-strain curves in uniaxial tension and/or compression. Poisson's ratio for mortar and for the aggregate particles is typically around 0.2 (Yurtdas, 2004). In this work the following values were used throughout: $\nu_m = 0.19$ and $\nu_\Omega = 0.21$. The volume fractions of the mortar and inclusion phase, f_m and f_Ω, can be determined from the mix proportions. If no or insufficient information is available to determine them, the recommended default values are $f_m = f_\Omega = 0.5$. Unless stated otherwise, the default values are employed in the numerical simulations presented here.

b) Fracture properties related to the crack initiation criterion and damage evolution (Section 2.4); these are: the tensile strength of the coarse aggregate–mortar matrix interface (f_{ti}) the crack opening at the effective end of the softening curve (u_0), parameter c_1 that controls the shape of the uniaxial tensile softening branch and the characteristic length (h). c_1 is equal to 5, unless stated otherwise, and h was fixed at $2 \cdot d_{agg}$ where d_{agg} is the maximum size of the coarse aggregate particles. For the uniaxial tension case in Example 1 the experimental strains were computed using the physical gauge length.

c) Contact parameters associated with the rough crack contact model (Section 2.5), i.e. the slope of the interlock surface (m_g), the opening strain at which shear contact is lost (ε_g) and the probability distributions $p_c(\varepsilon_g, m_g)$. These parameters provide a geometrical characterization of the crack surface roughness, m_g representing the slope of the surface asperities and ε_g the asperity height in strain terms (Mihai and Jefferson, 2013). Statistical distributions of slopes and heights of surface asperities can be determined from crack surface profiles and such attempts have been made by Boussa et al. (2001) and Lee et al. (2001). In this work a simple discrete distribution, given in Table

2, has been employed for all numerical simulations and the double integral in Equation (46) becomes a simple summation as follows:

$$\mathbf{C}_{\text{add}} = \left[\mathbf{C}_{\text{L}}{}^{-1} \cdot \left[(1-\omega)\mathbf{I}^{2\text{s}} + \omega \cdot \sum_i p_{ci} H(\boldsymbol{\varepsilon}_{\text{L}}, \varepsilon_{gi}) \boldsymbol{\Phi}(\boldsymbol{\varepsilon}_{\text{L}}, m_{gi}) \right] + \omega(1-\omega_f)\mathbf{D}_{\text{fl}} \right]^{-1} - \mathbf{C}_{\text{L}} \qquad (47)$$

in which p_{ci} is the proportion, or the probability of the occurrence, of a certain type of asperity. It is considered that $\sum_i p_{ci} < 1$ to account for the fact that the crack surface also contains very fine asperities that may not regain direct contact due to misalignments and loose material becoming lodged between opposing crack faces.

Table 2. Rough contact parameters

m_g	ε_g	p_c
3	$25\varepsilon_{ti}$	0.5
0.25	ε_0	0.23
0.8	ε_0	0.17

d) Fibre related parameters (Section 2.6); length and diameter of fibres (L_f and d_f), volume fraction of fibres (V_f), fibre-matrix interfacial properties (τ_0 and β) and the snubbing coefficient f_s. The geometrical properties and the content of fibres are material specifications rather than categorical model parameters and are readily obtained from the mix design specifications. τ_0 and β are parameters introduced in the pull-out model of Lin and Li (1997) and govern the assumed linear hardening behaviour of the fibre-matrix interface. Lin and Li (1997) provided direction on how these can be determined from single fibre pull-out tests. However, since data from pull-out tests are not provided in the experimental work used in the following sections to validate the model, the two fibre-matrix interface parameters were considered phenomenological.

A value of the snubbing coefficient of f_s = 0.75 was adopted for all numerical examples presented here, as recommended by Li et al. (1993) for steel fibres. It is noted that for nylon and polypropylene fibres in a normal mortar matrix values for the snubbing coefficient are reported to range between 0.5 and 1 (Li et al., 1990) whereas for steel fibres in a high strength matrix f_s can be as high as 1.6 (Lee et. al., 2010).

The probability density functions for the orientation and distribution of fibres relative to the crack-plane, $p(\varphi)$ and $p(z)$ in Equation (37), can also be regarded as model parameters. Uniform random distributions were considered for all examples presented in this work.

It can be noted that nearly all model parameters have a physical meaning and can be measured directly. Furthermore, their input values are kept constant for each set of simulations presented here with the exception of instances in which certain material constituents varied in the experimental tests e.g. fibre content, fibre geometry, mix design.

3.2. Example 1. Uniaxial tension tests of Li et al. (1998).

In this example, comparisons with data from uniaxial tension tests conducted by Li et al. (1998) on plain and steel fibre reinforced concrete specimens are presented. Li et al. (1998) carried out uniaxial tensile tests on plain and fibre reinforced concrete specimens with overall dimensions 350x100x20 mm, using linear variable displacement transducers (LVDTs) with a gauge length of 120 mm to measure the deformations. Two sets of experiments, employing two different types of steel fibres, were considered for comparison:

- straight Harex fibres with an arc cross-section (Set I)
- hooked-end Dramix fibres with a circular cross section (Set II).

For each set, uniaxial tensile responses were predicted for composites with fibre volume fractions of V_f = 0, 2, 3 and 6%.

The material properties employed that relate to the plain concrete are given in Table 3a and those related to the fibre-bridging component are presented in Table 3b. Li et al. (1998) reported that the concrete mix proportions were modified as the fibre content was increased in order to achieve sufficient workability. Water/cement ratio and cement dosage were kept constant for all mixes but the proportions of coarse aggregate decreased with increasing fibre content, with the result was that the initial stiffness decreased; mix A having the highest Young's modulus and mix C the lowest. The decreasing proportion of coarse aggregate particles, f_Ω, was taken into account in the model according to Table 3a and the values for E_m and E_Ω were chosen so that the Young's modulus of the plain cementitious composite would match the initial experimental stiffness. The only parameters that differ slightly between the two simulation sets are the fibre-matrix interface

properties, τ_0 and β. A higher value of τ_0 is used for numerical simulations in Set 1 compared to the value used for Set II as a means to account for the anchorage effect of the hooked Dramix fibres.

The numerical results compared with the experimental data are presented in Figure 7 for tests on specimens using Dramix fibres and in Figure 8 for Harex fibre specimens. A good correlation can be observed between the numerical predictions and the experimental results from a broad range of tests, involving different types of fibres and a wide range of fibre volume fractions. Li et al. (1998) provided a single experimental curve for each type of specimen however, it is noted that significant scatter of the experimental results has been reported in other tests on fibre reinforced composites (e.g. Parmentier et al., 2008). Taking this observation into account, and noting that all parameters - with the exception of τ_0 and f_Ω explained above - were kept constant throughout, a good degree of accuracy of the numerical predictions is observed. Therefore it can be concluded that the proposed model, combining the components detailed in Sections 2.2-2.6, is able to capture the characteristic behaviour of fibre reinforced cementitious composites in tension: the considerable increase in ductility and marginal increase in strength with increasing fibre content. Moreover, the model is able to simulate strain-hardening behaviour which is generally observed when higher volume fractions of fibres are used. When the material exhibits overall strain-hardening behaviour it may be expected that the microcracking zone widens, in contrast to the softening behaviour situation in which microcracks tend to coalesce in a narrow band and form a macro-crack (Naaman, 2008; Radtke et al., 2010).

Table 3a. Example 1. Material properties relating to plain concrete

Mix	V_f (%)	E_m (MPa)	E_Ω (MPa)	ν_m	ν_Ω	f_Ω	f_{ti} (MPa)	u_0 (mm)	h (mm)	c_1
A	2	25000	60000	0.19	0.21	0.5	1.5	0.125	120	10
B	3					0.25				
C	6					0.12				

Table 3b. Example 1. Material properties relating to fibre-bridging

Set/Fibre Type	L_f (mm)	d_f (mm)	E_f (MPa)	τ_0 (MPa)	β_f	f_s
Set I - Dramix	30	0.5	200000	0.8	0.1	0.75
Set II - Harex	32	0.8		0.6	0.08	

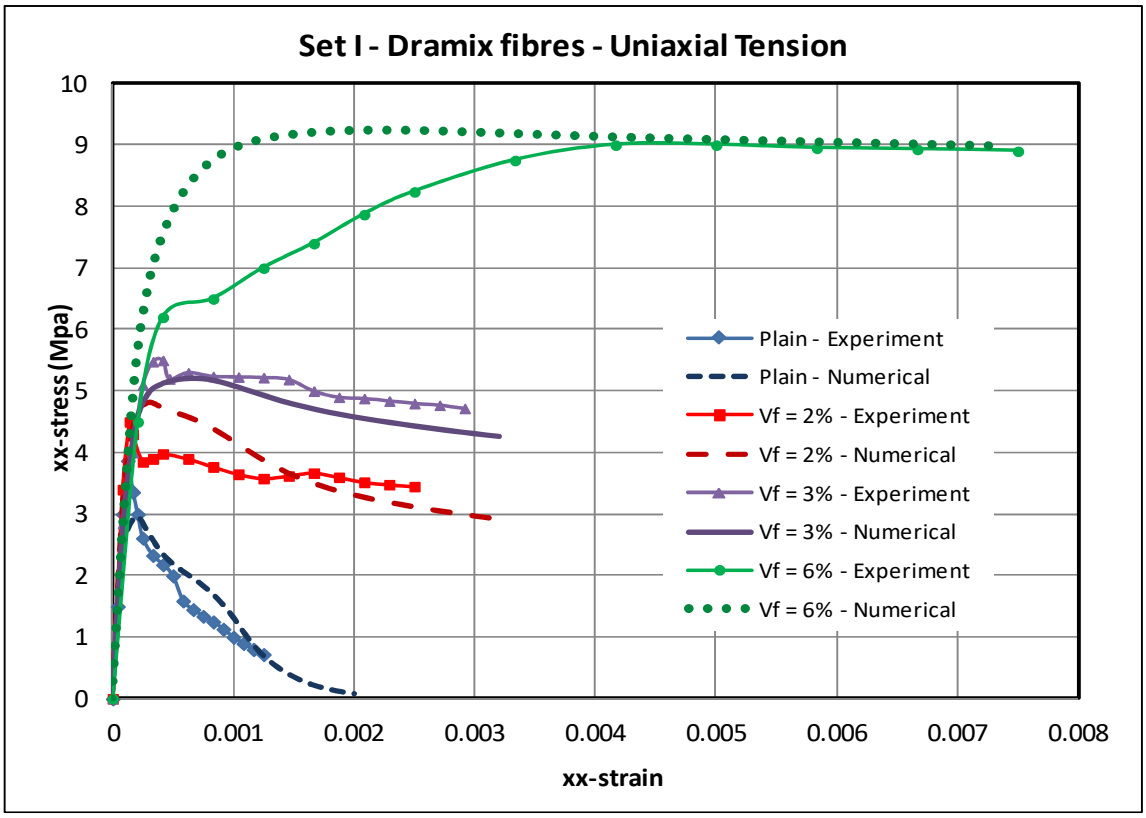

Figure 7. Numerical predictions of uniaxial tensile tests of Li et al. (1998) - Dramix fibres

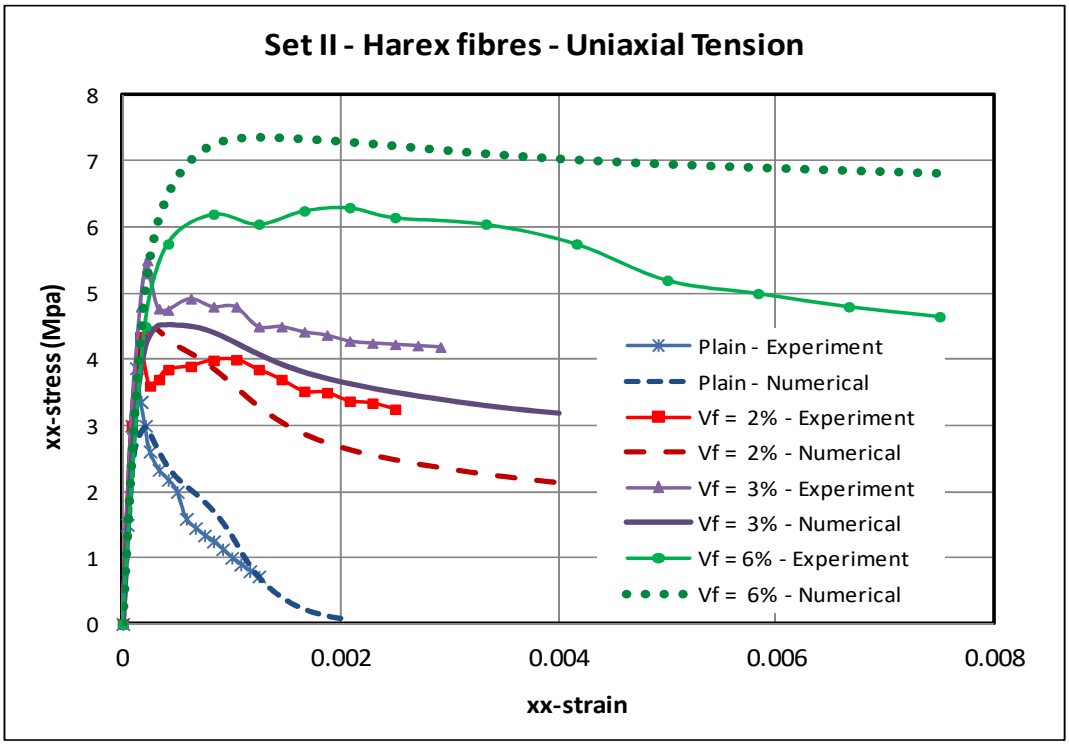

Figure 8. Numerical predictions of uniaxial tensile tests of Li et al. (1998) - Harex fibres

The constitutive model described in Section 2 captures the characteristic overall behaviour by employing mechanics based sub-models that simulate the key mechanisms that control the behaviour on crack-planes and subsequently integrating this crack-plane response from all directions. The model can also provide information regarding the degree of microcracking in each direction for different relative loading points. Such microcracking surface plots are presented in Figure 9 for the single-point simulation of the uniaxial tension test on FRC with 2% Dramix fibres at three different loading stages. The microcracking or damage surfaces are plotted in polar coordinates (ψ,ω), where ψ is the crack-plane orientation angle relative to the loading direction, defined in Figure 2 and ω is the directional damage parameter representing the degree of micro-cracking in each direction. These plots show the distribution of damage in each direction and its expansion as the applied strains increase. It can be seen that at post-peak stages b and c the concrete matrix is almost completely damaged and it is via the crack bridging action of fibres that the FRC material is able to sustain a significant level of load with increasing deformation.

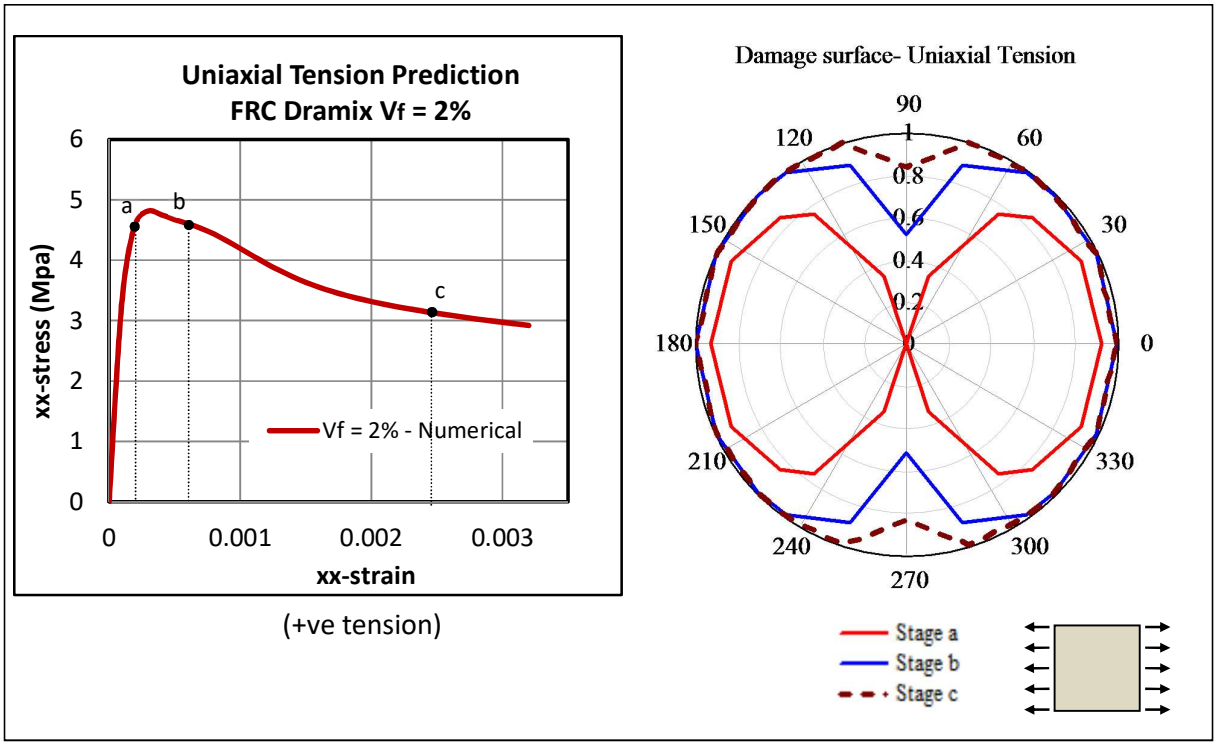

Figure 9. Damage surfaces – numerical simulation of the uniaxial tensile test on FRC 2% Dramix (Li et al., 1998)

3.3. Example 2. Uniaxial compression tests of Cachim et al. (2002)

In this example a comparison is presented between numerical simulations and experimental results from uniaxial compression tests conducted by Cachim et al. (2002) on 150x300mm (diameter x height) cylindrical plain and fibre reinforced concrete specimens. Two different series of fibre reinforced composites with identical concrete composition and volume fractions of fibres but different fibre types were used to form the specimens. The maximum size of the coarse aggregate particles was 15mm. 0.57% by volume of hooked-end steel fibres with overall dimensions of d_f = 0.5mm, L_f = 30mm for Series I and d_f = 0.8mm, L_f = 60mm for Series II were used respectively. Plain concrete specimens were also cast and tested in each Series. The ages of the Series I specimens were between 30 and 60 days whereas those of the Series II specimens were between 18-20 months. Therefore, despite the identical design mix, the concrete properties in each Series at the time of testing were different from each other; specimens in Series II had higher strength and elastic modulus than the specimens in Series I. This is reflected in numerical simulations by adopting higher values for f_{ti} and E_m in Series II than in Series I (Table 4a).

A summary of material properties for concrete and for fibres are given in Table 4a and 4b respectively. Numerical predictions for uniaxial compression compared with experimental data are presented in Figure 10 for Series I and Figure 11 for Series II. Cachim et al. (2002) presented between 4 and 6 experimental stress-strain curves for each type of specimens. For clarity, only the lower and upper experimental curves for each case are shown here. Furthermore, the damage surfaces at three different stages are shown in Figure 12 for the FRC uniaxial compression prediction of Series I test. This plot shows how damage increases both in terms of the magnitude of the damage parameter in any one given direction and the size of the angular band encompassing damaged directions

Table 4a. Example 2. Material properties relating to plain concrete

Series	E_m (MPa)	E_Ω (MPa)	ν_m	ν_Ω	f_{ti} (MPa)	u_0 (mm)	d_{agg}
I	17000	44000	0.19	0.21	1.5	0.43	15
II	32000				2		

Table 4b. Example 2. Material properties relating to fibre-bridging

Series	V_f (%)	L_f (mm)	d_f (mm)	E_f (MPa)	τ_0 (MPa)	β_f	f_s
I	0.57	30	0.5	200000	1.0	0.1	0.75
II		60	0.8				

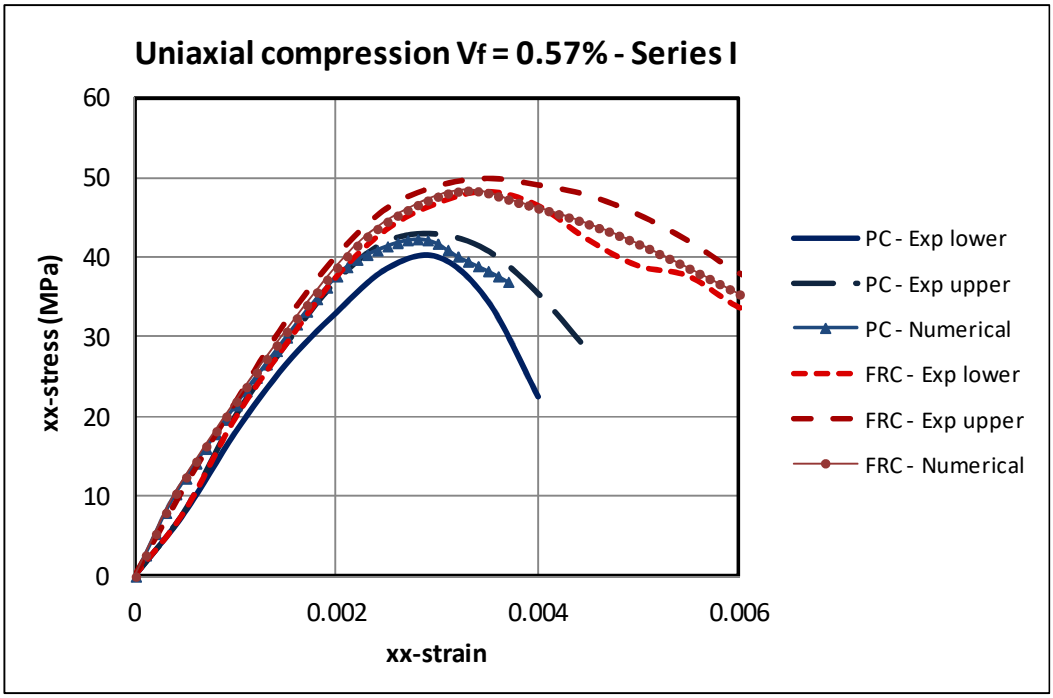

Figure 10. Numerical predictions of uniaxial compression tests of Cachim et al. Series I

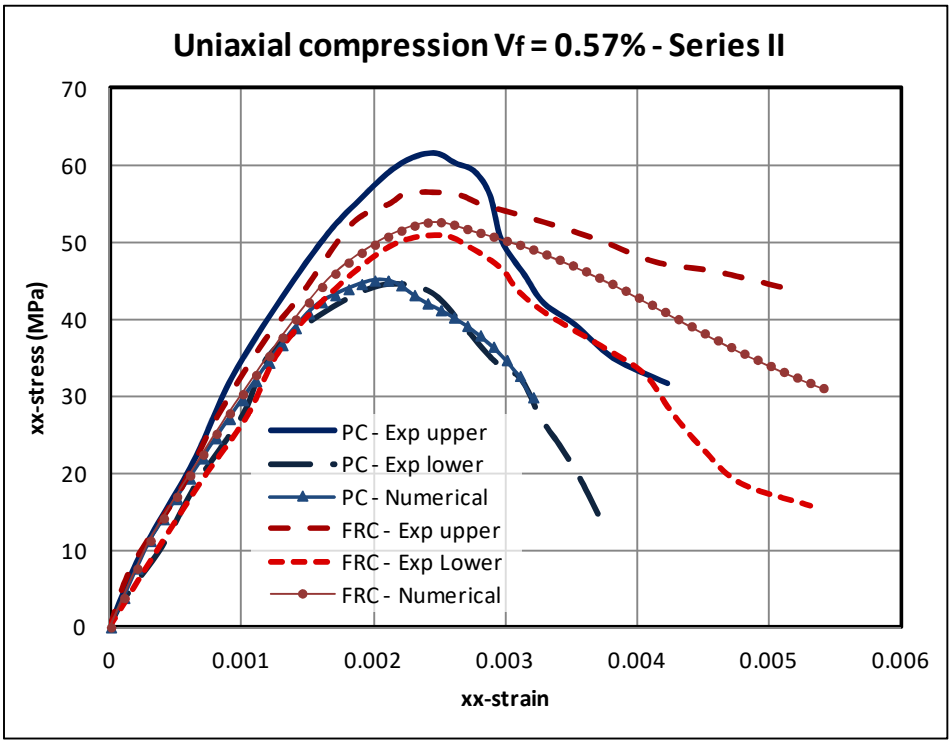

Figure 11. Numerical predictions of uniaxial compression tests of Cachim et al. Series II

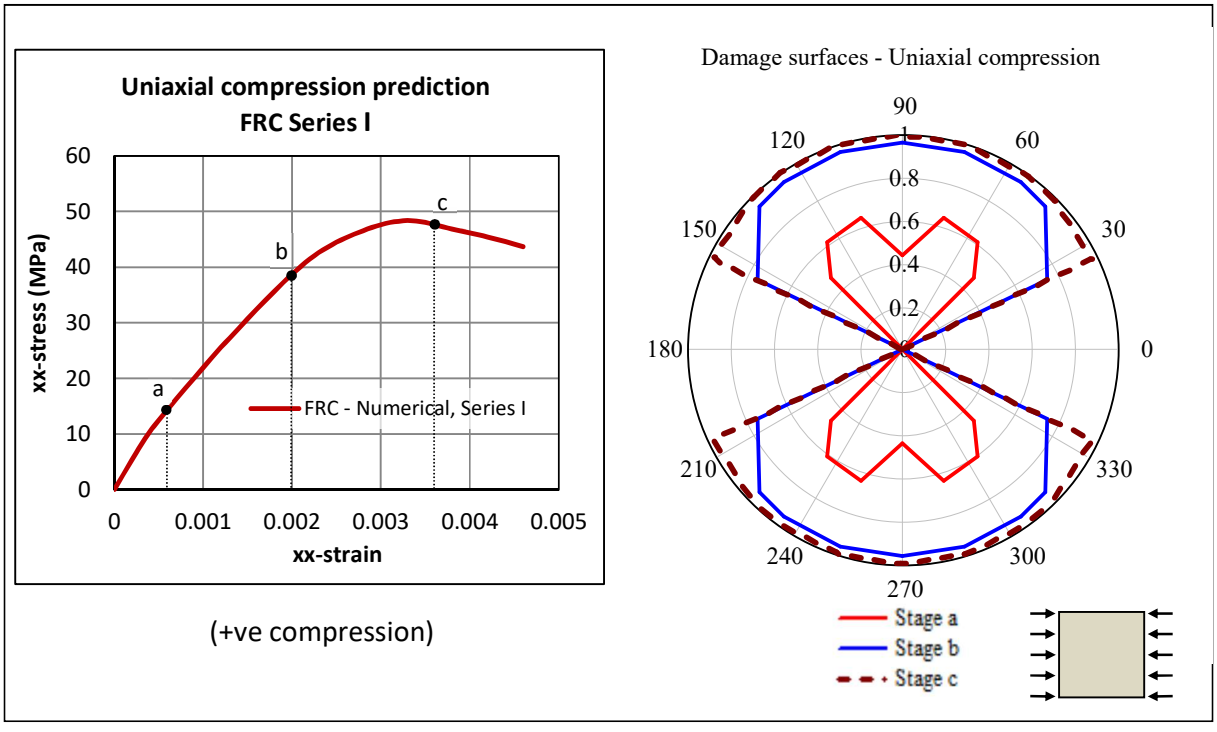

Figure 12. Damage surfaces – numerical simulation of uniaxial compression test of Cachim et al. (2002) Series I

For all cases the numerical predictions lie between experimental bounds and the model captures the slight increase in strength and an enhanced ductility of the FRC relative to plain concrete. Therefore it is concluded that the proposed micromechanics model is capable of predicting the characteristics of the tensile as well as compressive behaviour with the same formulation. This is in contrast to models following the more established phenomenological approach which generally require separate formulations to address tensile and compressive behaviour.

It is noted that the rough crack contact sub-model presented in Section 2.4 plays an important role in capturing the correct response in compression. To illustrate this, the uniaxial compression response predicted by the model for the uniaxial compressive tests in Series I with and without the contact component are compared in Figure 13. It can be observed that if rough contact is not taken into account the strength is significantly underestimated and the volumetric dilatancy is not captured at all.

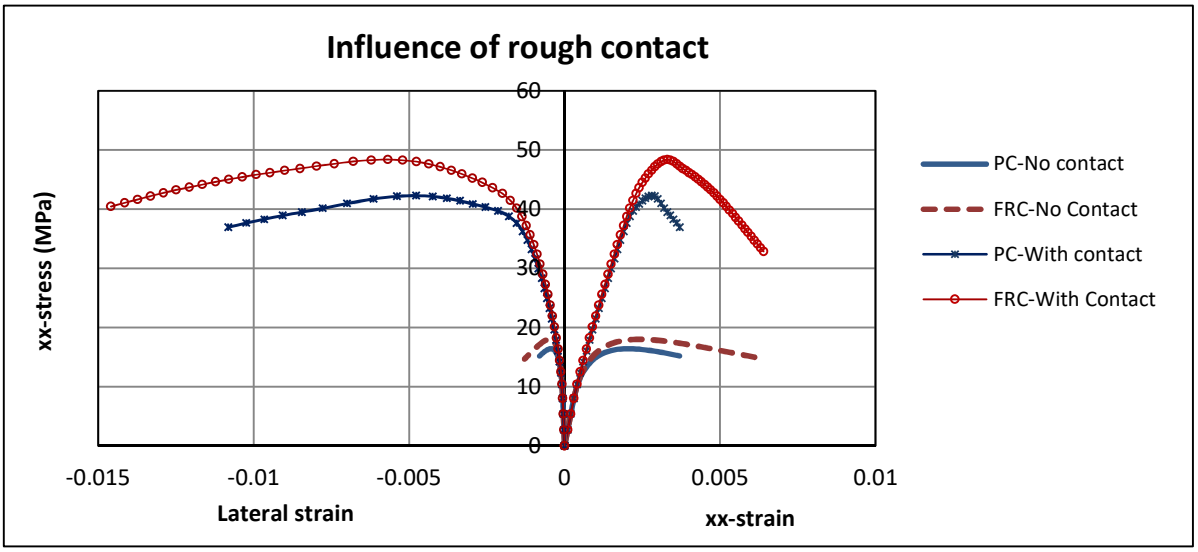

Figure 13. Uniaxial compression predictions with and without contact (+ve compression)

The sensitivity of the model to the rough contact parameters m_g and ε_g is shown in Figures 14 and 15 respectively for numerical simulations of uniaxial compressive tests in Series I. In these simulations, the values used for m_g and ε_g were varied by ± 10% relative to the nominal values from Table 2. The values of m_g and ε_g employed for the sensitivity studies and the predicted FRC strength values (f_{cf}), as well as those of the strain corresponding to the compressive strength (ε_{ccf}), are given in Table 5. Values of the remaining parameters are those given in Tables 4a and b.

Parameter m_g has a moderate influence on the predicted values of strength, with a variation of approximately 11% between the strength values from simulation S1 and simulation S3 respectively. A similar variation is noted for values of ε_{ccf}.

The model sensitivity to the variation of ε_g is more limited; the predicted strength values vary by 9% between *S4* and *S6* whereas the predicted values of ε_{ccf} vary by 12%.

As noted in 3.1.c), the values of the rough crack contact parameters have been fixed to those in Table 2 for all numerical examples.

Table 5. Contact sensitivity study. Contact parameters and related predictions of f_{cf} and ε_{ccf}

	$m_{g,i}$			$\varepsilon_{g,i}$			f_{cf} (MPa)	ε_{ccf}
S1 – 0.9 m_{g_av}	2.7	0.225	0.72	$25\varepsilon_{ti}$	ε_0	ε_0	51.2	0.0035
*S2 – 1.0*m_{g_av}	3	0.25	0.8				48.4	0.0033
*S3 – 1.1*m_{g_av}	3.3	0.275	0.88				45.7	0.0031
S4 – 0.9 ε_{g_av}	3	0.35	0.8	$22.5\varepsilon_{ti}$	0.9 ε_0	0.9 ε_0	46.4	0.0031
S5 – 1.0 ε_{g_av}				$25\varepsilon_{ti}$	1.0 ε_0	1.0 ε_0	48.4	0.0033
S6 – 1.1 ε_{g_av}				$27.5\varepsilon_{ti}$	1.1 ε_0	1.1 ε_0	50.6	0.0035

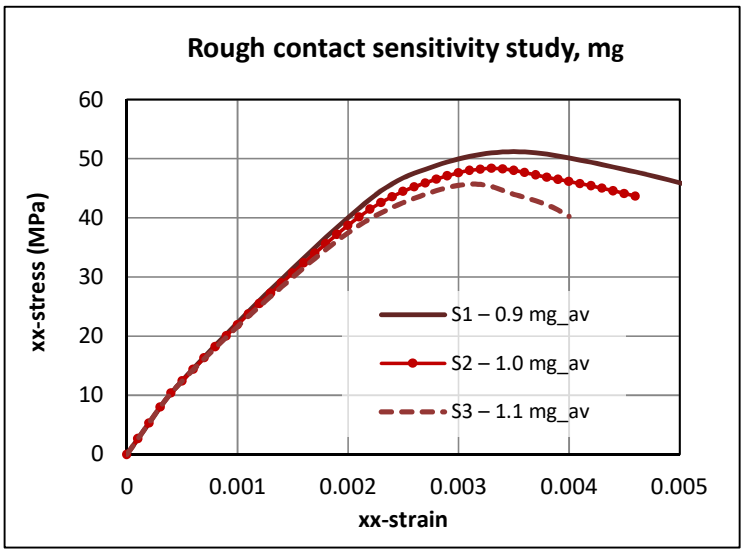

Figure 14. Influence of m_g contact parameter on the uniaxial compression response (+ve compression)

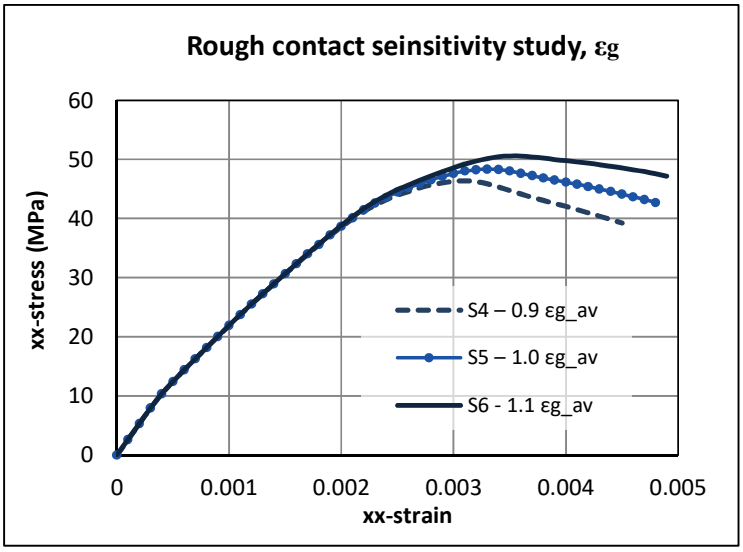

Figure 15. Influence of ε_g contact parameter on the uniaxial compression response (+ve compression)

3.4. Example 3. Biaxial compression test of Yin et al. (1989)

In this example numerical simulations of biaxial compressive behaviour of fibre reinforced concrete were carried out and the numerical predictions were compared with the experimental results of Yin et al. (1989). In the experimental study of Yin et al. (1989), plain and fibre reinforced concrete plates with dimensions of 152 x 152 x 38 mm were subjected to biaxial loading with various principal biaxial compression stress ratios.

A summary of material properties for concrete and for fibres are given in Table 6a and 6b respectively. Numerical predictions of the biaxial failure envelope compared with the experimental results are presented in Figure 16. f_{cp} denotes the uniaxial compressive strength of the plain concrete and $\sigma_1 > \sigma_2 > \sigma_3$ denote the principal stresses, with σ_2 and σ_3 corresponding to the loading directions.

Table 6a. Example 3. Material properties relating to plain concrete

E_m (MPa)	E_Ω (MPa)	ν_m	ν_Ω	f_{ti} (MPa)	u_0 (mm)	d_{agg} (mm)
30000	44000	0.19	0.21	1.9	0.275	9.5

Table 6b. Example 3. Material properties relating to fibre-bridging

V_f (%)	L_f (mm)	d_f (mm)	E_f (MPa)	τ_0 (MPa)	β_f	f_s
1	25	0.42	200000	*1.0*	*0.1*	0.75

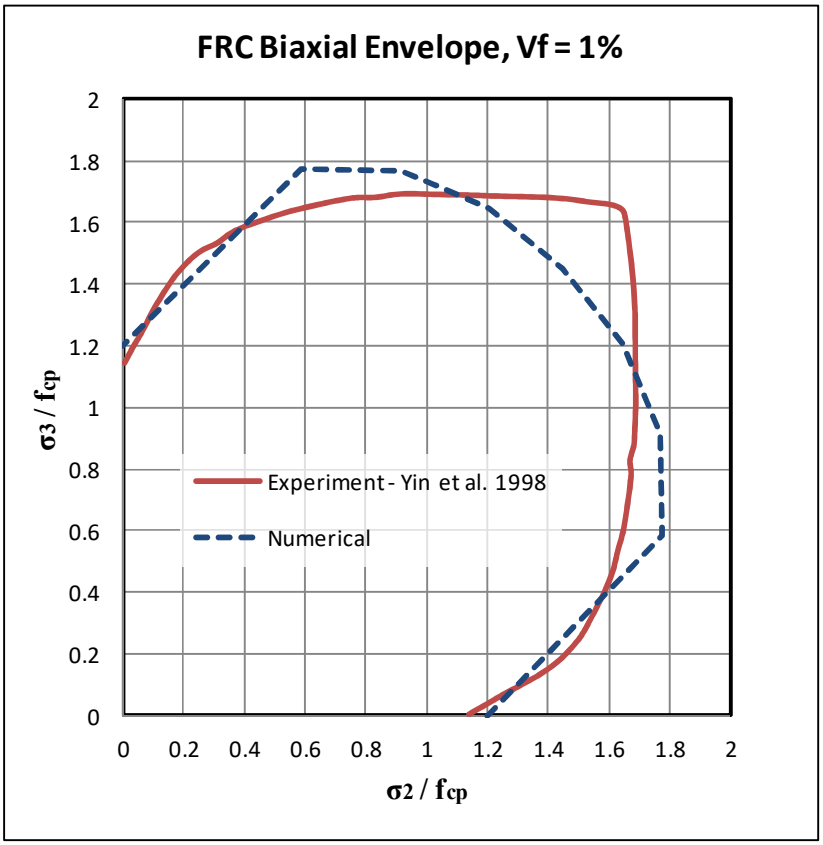

Figure 16. Numerical predictions of the biaxial strength envelope for FRC

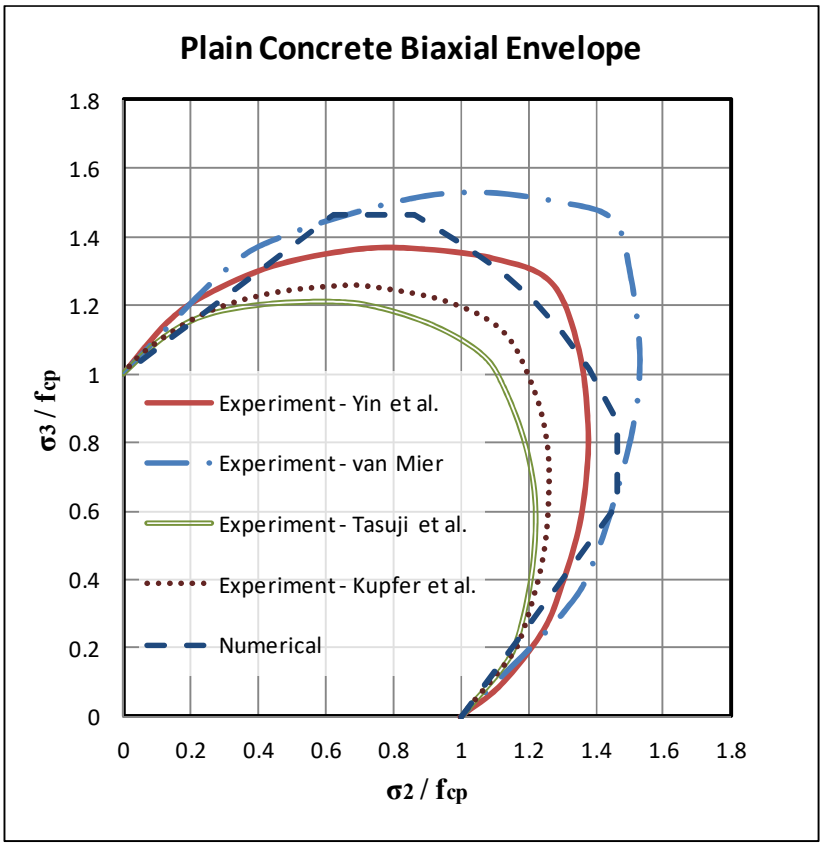

Figure 17. Numerical predictions of the biaxial strength envelope for FRC

The model captures the expansion of the strength envelope for FRC relative to plain concrete observed in experimental tests which essentially corresponds to an increase in strength with the addition of fibres. It would appear that the model overestimates strengths of FRC when the ratio of the principal stresses σ_2 / σ_3 is in the range of [0.25 - 0.5] and underestimates strengths for $\sigma_2 / \sigma_3 \in$ [0.8 – 1]. However, past experimental studies have shown a large scatter of results from tests on plain concrete specimens under multiaxial stress states which have been attributed primarily to variations of the material properties and testing methodology (Gertsle et al., 1978). This is illustrated in Figure 17 which shows experimental biaxial envelopes for plain concrete from several different studies (Kupfer et al., 1969; Tasuji et al., 1978; van Mier, 1986 and Yin et al., 1989) and the predicted biaxial envelope which is within experimental bounds. Given the considerable scatter of results observed in various uniaxial and bending tests (e.g. Cachim et al., 2002; Parmentier et al., 2008), the same reasoning can be readily extended to the present case of fibre reinforced cementitious composites subjected to biaxial stress states. Put in this context, the numerical predictions in Figure 16 are realistic although the tendency of the model to overestimate strengths for $\sigma_2 / \sigma_3 \in$ [0.25 –

0.5] is acknowledged. The current model does not account for plastic embedment, crushing or frictional sliding between asperities of opposing crack surfaces. Since these mechanisms become increasingly important as a specimen is more constrained, the authors believe that including them in the rough crack contact sub-model would improve the accuracy of the overall model for biaxial and triaxially confined stress/strain paths.

3.5. Example 4. Numerical simulations of triaxial compression

The performance of the model in compression under increasing levels of confinement is addressed here. The material parameters employed are given in Table 7 and the loading paths are presented in Figure 18. The model predictions of compression tests for three levels of confinement, 0 MPa, 5 MPa and 10 MPa respectively are presented in Figure 19. The model is able to capture the increase of compressive strengths with increasing levels of confinement as well as a substantial increase in ductility and the volumetric dilatancy characteristic of triaxial FRC behaviour under low to moderate levels of confinement.

The numerical predictions of triaxial strengths obtained for the three levels of confinement are compared with the experimental results obtained by Lu et al. (2006). These are shown in Figure 20 as f_{ct}/f_{c0} vs f_{cell}/f_{c0}; where f_{ct} is the triaxial strength or peak xx-stress, f_{c0} is the uniaxial compressive strength and f_{cell} is the confining pressure respectively. Comparisons with experimental data from Lu et al. (2006) of FRC specimens containing hooked fibres (V_f = 1% L_f = 30mm, d_f = 0.5mm) suggests that the model overestimates the triaxial strengths. As mentioned in 3.4, this is likely due to the fact that crushing and frictional sliding between the asperities on the crack faces are not directly represented in the rough contact model. Nevertheless, the variability of experimental results from tests on FRC is well documented, as is the fact that the experimental results are sensitive to the boundary conditions applied in tests and therefore more comprehensive experimental data would be needed for a more thorough qualitative comparison.

Table 7a. Example 4. Material properties relating to plain concrete

E_m (MPa)	E_Ω (MPa)	ν_m	ν_Ω	f_{ti} (MPa)	u_0 (mm)	d_{agg} (mm)
30000	44000	0.19	0.21	1.5	0.275	9.5

Table 7b. Example 4. Material properties relating to fibre-bridging

V_f (%)	L_f (mm)	d_f (mm)	E_f (MPa)	τ_0 (MPa)	β_f	f_s
1	30	0.5	200000	*1.0*	*0.1*	0.75

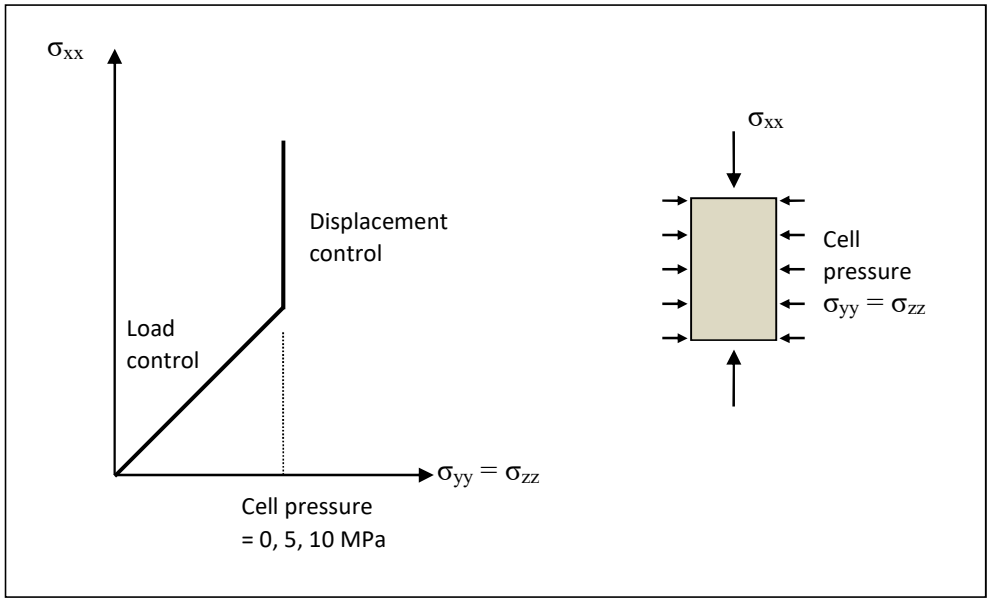

Figure 18. Triaxial simulations. Load paths

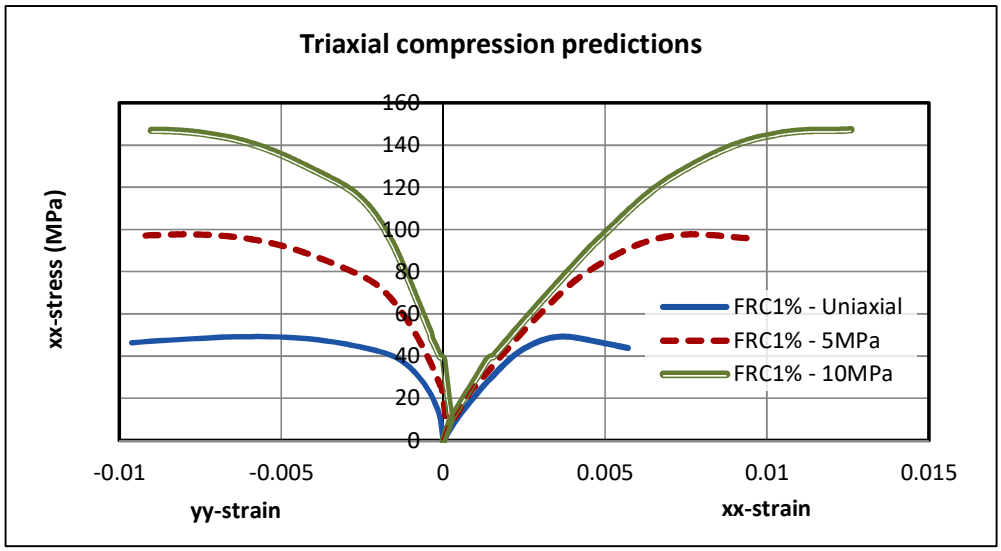

Figure 19. Numerical predictions of triaxial behaviour for FRC with 1% fibres

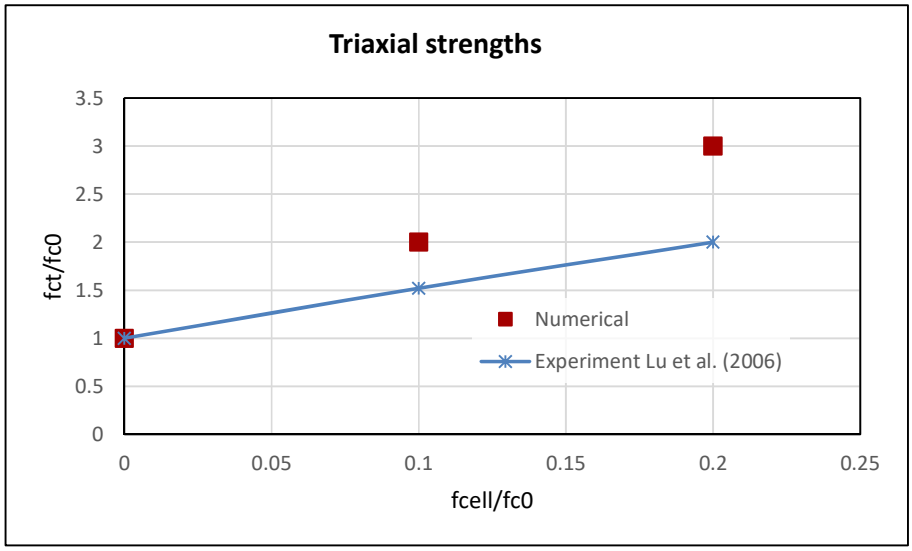

Figure 20. Numerical predictions of triaxial strengths for FRC with 1% fibres

3.6. Numerical integration.

Several numerical integration rules were employed to evaluate the sensitivity of model predictions to the order of the spherical integration used in the computations, i.e. to evaluate Equation 45, namely the Albrecht and Collatz 26 point rule, the Finden Sobolev and McLaren 32 point rule, the McLaren 42 point rule and the McLaren 50 point rule respectively (all referenced in Stroud, 1971). A uniaxial compression test undertaken by Cachim et al. (2002), previously considered in Section 3.3 of this paper, was used as the basis for the study. The results from simulations using the different integration rules are presented in Figure 21.

The results suggest that the 26 point rule has insufficient sample directions to capture any degradation of stiffness whereas the 32 point rule offers a better estimate but it is still incapable of capturing correctly the overall damage and consequently the degradation of stiffness and strength. In contrast it can be observed that the 42 point rule and the 50 point rule give converged results. All simulations presented in this paper employed McLaren 50 point rule (Stroud, 1971).

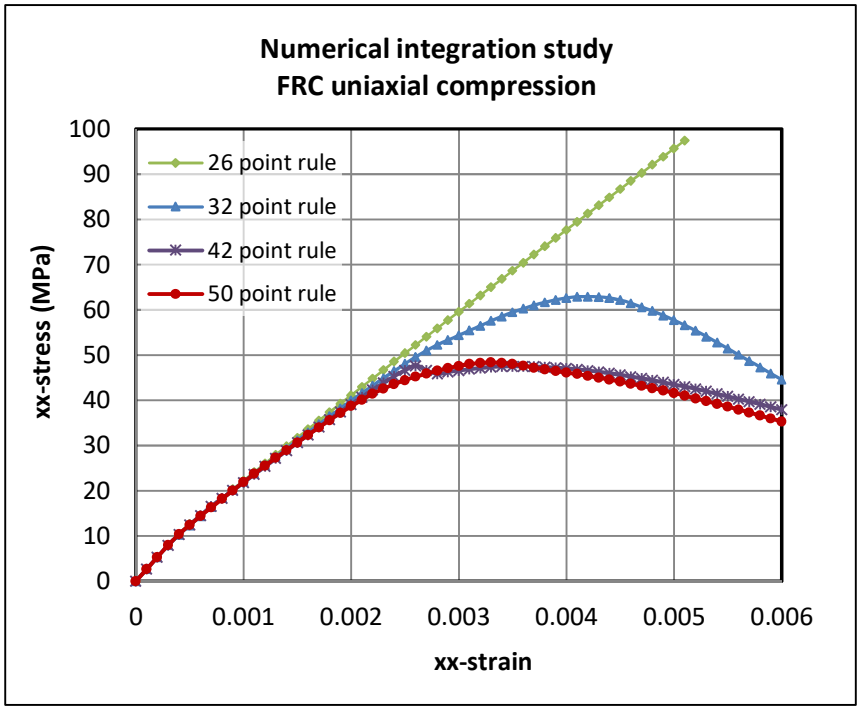

Figure 21. Numerical integration study for uniaxial compression

4. Conclusions

Micromechanical solutions can be employed to obtain average elastic properties of a composite based on the elastic properties of the constituent phases. These solutions are applied in a constitutive model for fibre-reinforced cementitious composites which is also able to simulate directional cracking, damage initiation in the interfacial transition zone between mortar and coarse aggregate particles, rough contact and the crack-bridging action of fibres.

Numerical predictions from single-point simulations of uniaxial tensile and uniaxial and biaxial compression tests show that the model captures correctly key characteristics of the complex mechanical behaviour of fibre reinforced cement based composites, such as the increase of ductility and overall toughness when fibres are added to the plain concrete matrix. Moreover, a single formulation, combining several sub-models that describe key physical mechanisms that in turn govern the mechanical response, is able to capture the fundamentally different behaviour in tension and compression respectively.

Acknowledgements

The authors gratefully acknowledge support for this work from both the TSB (INNOVATEUK) via KTP 8380 and the finite element company LUSAS.

REFERENCES

Abou-Chakra Guery A., Cormery F., Shao J.F. and Kondo D. **2008**. A micromechanical model of elastoplastic and damage behaviour of a cohesive geomaterial. *International Journal of Solids and Structures,* **45**: 1406-1429

Barros J.A.O. and Figueiras J.A. **1999**. Flexural behaviour of SFRC: Testing and modelling. *ASCE Journal of Materials in Civil Engineering*, **11**(4): 331-339

Bažant Z.P. and Oh B.H. **1983**. Crack band theory for fracture in concrete. *Materials and Structures*, **16**: 155-177.

Beghini A., Bažant Z.P., Zhou Y., Gouirand O and Caner F.C. **2007**. Microplane model M5f for multiaxial behaviour and fracture of fiber-reinforced concrete. *ASCE Journal of Engineering Mechanics*, **133**(1):66-75

Bernard O., Ulm F.J. and Lemarchand E. **2003.** A multiscale micromechanics-hydration model for the early-age elastic properties of cement-based materials. *Cement and Concrete* Research **33**: 1293 – 1309

Bolander J.E., Choi S. And Duddukuri S.R. **2008**. Fracture of fiber-reinforced cement composites: effects of fibre dispersion. *International Journal of Fracture,* **154**: 73-86

Bolander J.E. and Saito S. **1997**. Discrete modelling of short-fiber reinforcement in cementitious composites. *Advanced Cement Based Materials,* **6**: 76-86

Boussa H., Tognazzi-Lawrence C. and La Borderie C. **2001**. A model for computation of leakage through damaged concrete structures. *Cement & Concrete Composites*, **23**: 279-287

Boyd G.J. and Lagoudas D.C. **1996**. A thermodynamical constitutive model for shape memory materials. Part II. The SMA composite material. *International Journal of Plasticity,* **12**(7): 843-873

Budiansky B. and O'Connell R.J. **1976**. Elastic moduli of a cracked solid. *International Journal of Solids and Structures,* **12**: 81-97

Cachim P.B., Figueiras J.A. and Pereira P.A.A. **2002**. Fatigue behaviour of fiber-reinforced concrete in compression. *Cement & Concrete Research,* **24**: 211-217

Caner F.C., Bažant Z.P. and Wendner R. **2013**. Microplane model M7f for fiber reinforced concrete. *Engineering Fracture Mechanics*, **105**:41-57

Chaboche J.L., Kruch S., Marie J.F. and Pottier T. **2001**. Towards a micromechanics based inelastic and damage modeling of composites. *International Journal of Plasticity,* **17**(4): 411-439

Cunha V.M.C.F., Barros J.A.O. and Seva-Cruz J.M. **2012**. A finite element model with discrete embedded elements for fibre reinforced composites. *Computers and Structures,* **94-95**: 22-33

Davies R. and Jefferson A.D. **2015**. The simulation of inelastic matrix strains in cementitious materials using micromechanical solutions. *Engineering Fracture Mechanics*, **133**: 191–210

Eshelby J.D. **1957**. The determination of the elastic field of an ellipsoidal inclusion, and related problems. *Proceedings of the Royal Society of London. Series A, Mathematical and Physical Sciences*, **241** : 376-396

Ezeldin A.S. and Balaguru P.N. **1992**. Normal- and high- strength fiber reinforced concrete under compression. *ASCE Journal of Materials in Civil Engineering,* **4**(4): 415-429

Ferrara L., Park Y-D. and Shah S.P. **2008**. Correlation among fresh state behaviour, fiber dispersion and toughness properties of SFRCs. *ASCE Journal of Materials in Civil Engineering,* **20**: 493-501

Gambarotta L. **2004**. Friction-damage coupled model for brittle materials. *Engineering Fracture Mechanics,* **71**: 824-836

Garg S.K., Svalbonas V. and Gurtman G.A. **1973** *Analysis of Structural Composite Materials*. Marcel Dekker, Inc. New York

Gerstle K.H., Linse D.L., Bertacchi P., Kotosovos M.D., Ko H.-Y., Newman J.B., Rossi P., Schickert G., Taylor M.A, Traina L.A., Zimmerman R.M. and Bellotti R. **1978**. Strength of concrete under multiaxial stress states, in *Proceedings Douglas McHenry International Symposium on 'Concrete and Concrete Structures', ACI SP 55, American Concrete Institute*, Detroit, Mi, 103-131

Gopalaratnam V.S. and Shah S.P. **1987**. Tensile failure of steel fiber-reinforced mortars. *ASCE Journal of Engineering Mechanics*, **113**(5): 635-652.

Habel K., Viviani M., Denarie E. and Bruhwiler E. **2006**. Development of the mechanical properties of an Ultra-High Performance Fiber Reinforced Concrete (UHPFRC). *Cement and Concrete Research,* **36**(7): 1362-1370.

Hameed R., Sellier A., Turatsinze A. and Duprat F. **2013**. Metallic fiber-reinforced concrete behaviour: Experiments and constitutive law for finite element modelling. *Engineering Fracture Mechanics*, **103**: 124-131

Issa M.A., Issa M.A., Islam Md. S. and Chudnovsky A. **2003**. Fractal dimension—a measure of fracture roughness and toughness of concrete. *Engineering Fracture Mechanics*, **70**: 125–137

Jefferson A.D. **2002**. A constitutive model for aggregate interlock on formed crack planes. *International Journal of Numerical and Analytical Methods in Geomechanics* **26**: 1-21

Jefferson A.D. **2003**. Craft – a plastic-damage-contact modl for concrete. I. Model theory and thermodynamic considerations. *International Journal of Solids and Structures* **40**: 5973-5999

Jefferson A.D. and Bennett T. **2007**. Micro-mechanical damage and rough crack closure in cementitious composite materials. *International Journal for Numerical and Analytical Methods in Geomechanics,* **31**: 133-146

Jefferson A.D. and Bennett T. **2010**. A model for cementitious composite materials based on micro-mechanical solutions and damage-contact theory. *Computers and Structures,* **88**: 1361-1366

Ju J.W. and Lee H.K. **2000**. A micromechanical damage model for effective elastoplastic behaviour of ductile matrix composites considering evolutionary complete particle debonding. *Computer Methods in Applied Mechanics and Engineering,* **183**(3/4): 201-222

Ju J.W. and Lee H.K. **2001**. A micromechanical damage model for effective elastoplastic behaviour of partially debonded ductile matrix composites. *International Journal of Solids and Structures,* **38**: 6307-6332

Ju J.W. and Lee X. **1991**. Micromechanical damage models for brittle solids. I: Tensile loadings. *ASCE Journal of Engineering Mechanics*, **117**(7):1495–1514.

Ju J.W. and Sun L.Z. **2001**. Effective elastoplastic behaviour of metal matrix composites containing randomly located aligned spheroidal inhomogeneities. Part I: micromechanics-based formulation. *International Journal of Solids and Structures,* **38**: 183-201

Ju J.W. and Sun L.Z. **1999**. A Novel Formulation for the Exterior-Point Eshelby's Tensor of an Ellipsoidal Inclusion. *Journal of Applied Mechanics, ASME,* **66**: 570 – 574

Kabele P. **2003**. New developments in analytical modeling of mechanical behaviour of ECC. *Journal of Advanced Concrete Technology,* **1**(3): 253-264

Kabele P. **2007**. Multiscale framework for modelling of fracture in high performance fiber reinforced cementitious composites. *Engineering Fracture Mechanics,* **74**: 194-209

Kang J., Kim K., Lim Y.M. and Bolander J.E. **2014.** Modeling of fiber-reinforced cement composites: Discrete representation of fiber pullout. *International Journal of Solids and Structures*, **51**(10): 1970–1979

Karihaloo B.L. and Wang J. **2000**. Mechanics of fibre-reinforced cementitious composites. *Computers and Structures,* **76**: 19-34

Karihaloo B.L., Wang J. and Grzybowski M. **1996**. Doubly periodic arrays of bridged cracks and short fibre reinforced cementitious composites. *Journal of the Mechanics and Physics of Solids,* **44**(10): 1565-1586

Kholmyansky M.M. **2002**. Mechanical resistance of steel fiber reinforced concrete to axial load. *ASCE Journal of Materials in Civil Engineering*, **14**(4): 311-319

Kullaa J. **1994**. Constitutive modelling of fiber-reinforced concrete under uniaxial tensile loading. *Composites,* **25**(10): 935-944

Kupfer H.B., Hilsdorf H.K., Ruch H. **1969**. Behaviour of concrete under biaxial stresses. *Journal of the ACI*, **66**(8): 656-666

Lange-Kornbak D. and Karihaloo B.L. **1997**. Tension softening of fibre-reinforced cementitious composites. *Cement and Concrete Composites*, **19**(4): 285-389

Lee H.S., Park I.J., Cho T.F. and You K.H. **2001**. Influence of asperity degradation on the mechanical behaviour of rough rock joints under cyclic shear loading. *International Journal of Rock Mechanics and Mining Sciences,* **38**: 967-980

Lee X. and Ju J.W. **1991**. Micromechanical damage models for brittle solids. II: Compressive loadings. *ASCE Journal of Engineering Mechanics,* **117**(7):1515–1536.

Lee Y., Kang S.T. and Kim J.K. **2010**. Pullout behavior of inclined steel fiber in an ultra-high strength cementitious matrix. *Construction and Building Materials*, **24**: 2030–2041

Li F. and Li Z. **2001**. Continuum damage mechanics based modeling of fiber reinforced concrete in tension. *International Journal of Solids and Structures*, **38**: 777–793

Li S., Sauer R.A. and Wang G. **2007**. The Eshelby Tensors in a Finite Spherical Domain – Part I: Theoretical Formulations. *Journal of Applied Mechanics, ASME,* **74**: 770 – 783

Li V.C. **1992**. Postcrack scaling relations for fiber reinforced cementitious composites. *ASCE Journal of Materials in Civil Engineering*, **4**(1):41–57 .

Li V.C. **1998**. Engineered cementitious composites (ECC) – Tailored composites through micromechanical modeling. *Fiber Reinforced Concrete: Present and the Future*, Eds: N. Banthia, A. Bentur, and A. Mufti, Canadian Society of Civil Engineers, Montreal, 64-97.

Li V.C. **2003**. On engineered cementitious composites (ECC). A review of the material and its applications. *Journal of Advanced Concrete Technology,* **1**(3): 215-230

Li V.C., Stang H. and Krenchel H. **1993.** Micromechanics of crack bridging in fibre-reinforced concrete. *Materials and Structures*, **26**: 486-494

Li V.C., Wang Y. and Backer S. **1990**. Effect of inclining angle, bundling and surface treatment on synthetic fibre pull-out from a cement matrix. *Composites,* **21**(2):132-140

Li V.C., Wang Y. and Backer S. **1991**. A micromechanical model of tension-softening and bridging toughening of short random fiber reinforced brittle matrix composites. *Journal of the Mechanics and Physics of Solids,* **39**(5): 607-625

Li Z., Li F., Chang T.-Y.P. and Mai Y.-W. **1998**. Uniaxial tensile behaviour of concrete reinforced with randomly distributed short fibres. *ACI Materials Journal,* **95**(5): 564-574

Lim T. Y., Paramasivam P. and Lee S. L. **1987**. Analytical model for tensile behaviour of steel-fiber concrete. *ACI Materials Journal***, 84**(4): 286-298

Lin Z. and Li V.C. **1997**. Crack bridging in fiber reinforced cementitious composites with slip-hardening interfaces. *Journal of the Mechanics and Physics of Solids,* **45**(5): 763-787

Lu X. and Hsu C-T. T. **2006.** Behavior of high strength concrete with and without steel fiber reinforcement in triaxial compression. *Cement and Concrete Research* **36**: 1679–1685

Luccioni B., Ruano G., Isla F., Zerbino R. and Giaccion G. **2012**. A simple approach to model SFRC. *Construction and Building Materials*, **37**: 111-124

Mandel J.A., Wei S. and Said S. **1987**. Studies of the properties of the fiber-matrix interface in steel fiber reinforced mortar. *ACI Materials Journal***, 84**(2):101-109

Mihai I.C. and Jefferson A.D. **2011**. A numerical model foe cementitious composite materials with an exterior point Eshelby microcrack initiation criterion. *International Journal of Solids and Structures,* **48**: 3312-3325

Mihai I.C. and Jefferson A.D. **2013**. A multi-asperity plastic-contact crack plane model for geomaterials. *International Journal for Numerical and Analytical Methods in Geomechanics,* **37**(11): 1492–1509

Mura T. **1987**. *Micromechanics of Defects in Solids.* Second, revised edition, Martinus Nijoff Publishers, The Netherlands

Naaman A.E. **2008.** Development and evolution and of tensile strain-hardening FRC composites. *7th International RILEM Symposium on Fibre Reinforced Concrete: Design and Applications. BEFIB-2008, Chennai, India; 1-28*

Naaman A.E. **2011**. Half a century of progress leading to ultra-high performance finer-reinforced concrete: Part I – Overall review. *Proceedings of the 2nd International RILEM Conference on Strain Hardening Cementitious Composites, Rio de Janeiro, Brazil 2011*: 17-26

Naaman A.E., Namur G.G., Alwan J.M. and Najm H.S. **1991**. Fiber pullout and bond slip. I: Analytical study. *ASCE Journal of Structural Engineering*, **117**(9): 2769-2790

Naaman A.E., Namur G.G., Alwan J.M. and Najm H.S. **1991**. Fiber pullout and bond slip. II: Experimental validation. *ASCE Journal of Structural Engineering*, **117**(9): 2791-2800

Nataraja M.C., Dhang N. and Gupta A.P. **1999**. Stress-strain curves for steel-fiber reinforced concrete under compression. *Cement & Concrete Composites* **21**: 383-390

Nemat-Nasser S. and Hori M. **1993**. *Micromechanics: Overall Properties of Heterogeneous Materials*. Amsterdam: North-Holland

Nichols A.B. and Lange D.A. **2006**. 3D surface image analysis for fracture modelling of cement based materials. *Cement and Concrete Research* **36**: 1098-1107

Oliver J., Mora D.F., Husepe A.E. and Weyler R. **2012**. A micromorphic model for steel fiber reinforced concrete. *International Journal for Solids and Structures*, **49**(21): 2990-3007

Parmentier B., Vandewalle L. and Van Rickstal F. **2008**. Evaluation of the scatter of the postpeak behaviour of fibre reinforced concrete in bending: A step towards reliability. *7th International Symposium on Fibre Reinforced Concrete: Design and Applications, 133- 143*

Peng X. and Meyer C. **2000**. A continuum damage mechanics model for concrete reinforced with randomly distributed short fibers. *Computers and Structures*, **78**: 505-515

Pensee V. and Kondo D. **2003**. Micromechanics of anisotropic brittle damage: comparative analysis between a stress based and a strain based formulation. *Mechanics of Materials,* **35**: 747-761

Pensee V., Kondo D. and Dormieux L. **2002**. Micromechanical analysis of anisotropic damage in brittle materials. *ASCE Journal of Engineering Mechanics*, **128**(8): 889-897

Pichler B., Hellmich C. **2011**. Upscaling quasi-brittle strength of cement paste and mortar: a multi-scale engineering mechanics model. *Cement and Concrete Research*; **41**(5):247–476.

Pichler B., Hellmich C., Eberhardsteiner J., Wasserbauer J., Termkhajornkit P., Barbarulo R., Chanvillardb G. **2013.** Effect of gel–space ratio and microstructure on strength of hydrating

cementitious materials: an engineering micromechanics approach. *Cement and Concrete Research,* **45**:55–68.

Pichler C., Lackner R., Mang H.A. **2007**. A multiscale micromechanics model for the autogenous-shrinkage deformation of early-age cement-based materials. *Engineering Fracture Mechanics*, **74**(1–2):34–58.

Pichler C., Lackner R. **2008** A multiscale creep model as basis for simulation of early age concrete behaviour. *Computers and Concrete*, **5**(4):295–328.

Radtke F.K.F., Simone A. and Sluys L.J. **2010**. A computational model for failure analysis of fibre reinforced concrete with discrete treatment of fibres. *Engineering Fracture Mechanics*, **77**: 597-620

Ravichandran G. and Liu C.T. **1995**. Modeling constitutive behaviour of particulate composites undergoing damage. *International Journal of Solids and Structures,* **32**(6/7): 979-990

Schauffert E.A. and Cusatis G. **2012**. Lattice discrete particle model for fiber-reinforced concrete. I: Theory. *ASCE Journal of Engineering Mechanics*, **138**(7): 826-833

Schauffert E.A., Cusatis G., Pelessone D., O'Daniel J.L. and Baylot J.T. **2012.** Lattice discrete particle model for fiber-reinforced concrete. II: Tensile fracture and multiaxial loading behaviour. *ASCE Journal of Engineering Mechanics*, **138**(7): 834-841

Soroushian P. and Lee C.D. **1989**. Constitutive modelling of steel fiber reinforced concrete under direct tension and compression. *Fibre reinforced cements and concretes, recent developments,* Swamy R.N. and Barr B. eds., 1989: 363-375.

Stang H., Li Z. and Shah S.P. **1990**. Pullout problem: stress versus fracture mechanical approach. *ASCE Journal of Engineering Mechanics*, **116** (10): 2136-2150

Stroud A.H. **1971**. *Approximate calculation of multiple integrals*. Prentice-Hall, Inc

Sun L.Z. and Ju J.W. **2001**. Effective elastoplastic behaviour of metal matrix composites containing randomly located aligned spheroidal inhomogeneities. Part II: applications. *International Journal of Solids and Structures,* **38**: 203-225

Tasuji M.E., Slate F.O. and Nilson A.H. **1978**. Stress-strain response and fracture of concrete in biaxial loading. *ACI Journal, Proceedings*, **75**(7):306-312

van Mier, J.G.M. **1986**. Fracture of concrete under complex stress, *Heron* **31**(3): 1-90

Wei S., Mandel J.A. and Said S. **1986**. Studies of the interface strength in steel fiber-reinforced cement-based composites. *ACI Materials Journal***, 83**(4): 597-605

Yang, C.C. **1998**. Effect of the transition zone on the elastic moduli of mortar. *Cement and Concrete Research*, **28**(5): 727-736

Yin W.S., Su E.C.M., Mansur M.A. and Hsu T.T.C. **1989.** Biaxial test of plain and fiber concrete. *ACI Materials Journal,* **86**(3): 236-243

Yurtdas I., Burlion N., Skoczylas F. **2004**. Experimental characterization of the drying effect on uniaxial mechanical behaviour of concrete. *Materials and Structures,* **37**: 170-176

Zampini D., Jennings H.M and Shah S.P. **1995.** Characterization of the paste-aggregate interfacial transition zone surface roughness and its relationship to the fracture toughness of concrete. *Journal of material Science,* **30**(12): 3149-3154

Zhan Y. and Meschke G. **2014.** Analytical model for the pullout behavior of straight and hooked-end steel fibers. *ASCE Journal of Engineering Mechanics*, **140** (12): 04014091

Zhu Q.Z., Kondo D. and Shao J.F. **2008**. Micromechanical analysis of coupling between anisotropic damage and friction in quasi brittle materials: Role of homogenization scheme. *International Journal of Solids and Structures,* **45**: 1358-1405

Zhu Q.Z., Kondo D. and Shao J.F. **2009**. Homogenization-based analysis of anisotropic damage in brittle materials with unilateral effect and interactions between microcracks. *International Journal for Numerical and Analytical Methods in Geomechanics,* **33**: 749-772

Zhu Q.Z. and Shao J.F. **2015**. A refined micromechanical damage-friction model with strength prediction for rock-like materials under compression. *International Journal of Solids and Structures*, **60-61**: 75-83

Zhu Q.Z., Zhao L.Y. and Shao J.F. **2016**. Analytical and numerical analysis of frictional damage in quasi-brittle materials. *Journal of the Mechanics and Physics of Solids*, **92**:137-163